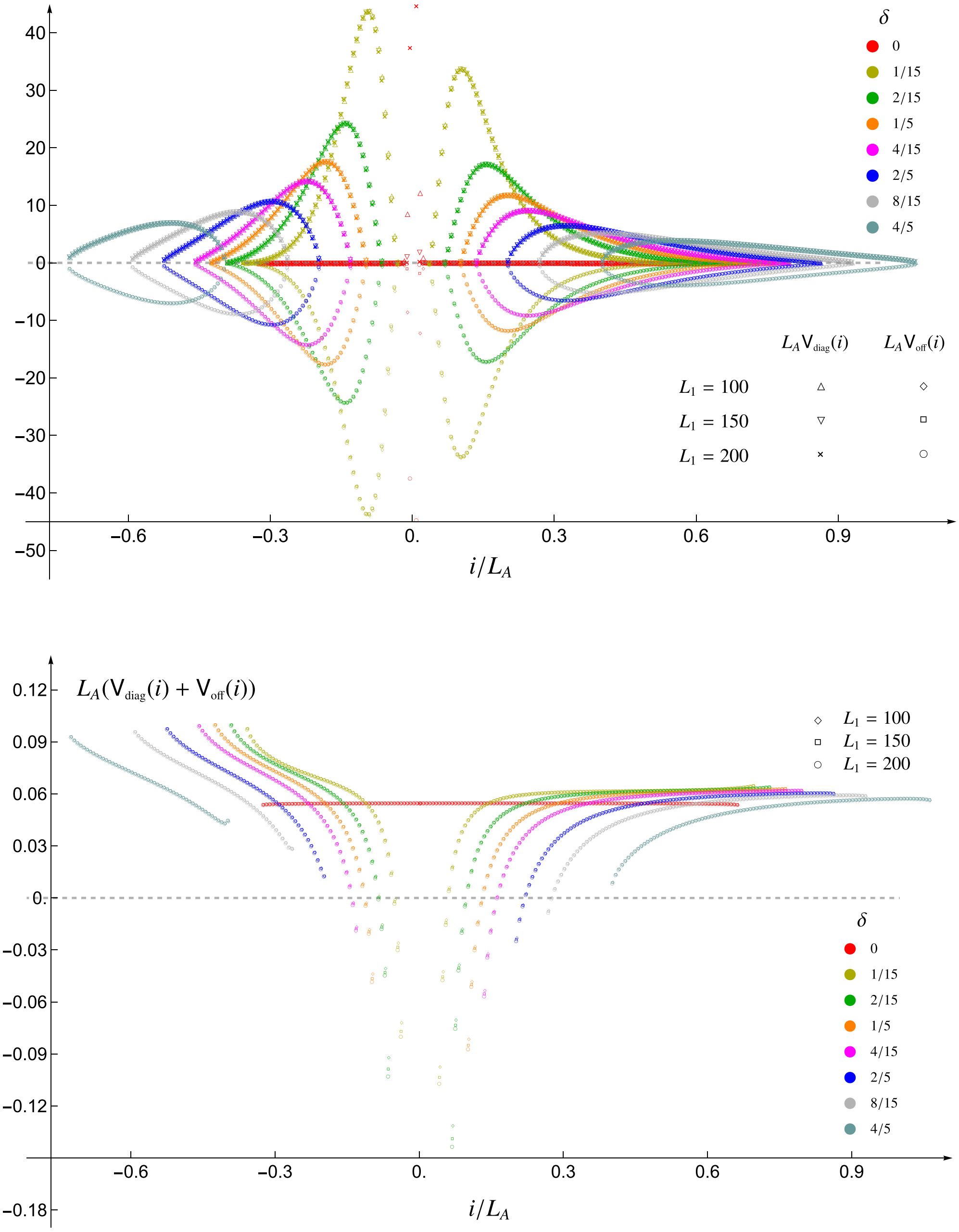

Figure 19. Combinations of elements in V defined in (7.13) and (7.14), for $L_2 = 2L_1$.

Moreover, the curves in the top panel of figure 19 display the same qualitative behaviour of $\left|\beta_{\text{biloc}}(x)\right|$, where $\beta_{\text{biloc}}(x)$ is the weight function (B.5) occurring in the bi-local term (B.4), found in [22] for a massless Dirac field. The special case of adjacent intervals can be understood by employing *e.g.* the panel about the matrix V corresponding to $\omega = 10^{-30}$ in figure 10 of [21].

Given the results of [23] for the fermionic case (see also appendix B), we conclude that the collapses observed in figures 18 and 19 strongly indicate that a non-local term should occur in the entanglement Hamiltonian of a massless scalar field, but we cannot establish whether this term is bi-local, like in the fermionic case of [22] (see (B.4)–(B.6)), or fully non-local, like in the case of the free chiral current model considered in [28] (see also section 8).

It is worth exploring the local term of the entanglement Hamiltonian in the continuum limit by adapting to our case the method developed in [12–15, 17] for a single block in infinite free chains (see [16] for the higher dimensional case of the ball), which has provided the corresponding CFT results [8, 9].

This local term originates from the diagonal blocks in T and V. As a first step of this analysis, we consider the thermodynamic limit of the kth diagonal of these diagonal blocks, namely

$$\lim_{L_A\to\infty}\frac{T_{i,i+k}}{L_A}\equiv\tau_k\left(x_k\right)\qquad\qquad \lim_{L_A\to\infty}\frac{V_{i,i+k}}{L_A}\equiv\nu_k\left(x_k\right)\qquad\qquad x_k\equiv\frac{1}{L_A}\left(i+\frac{k}{2}\right)\tag{7.15}$$

where $i+k/2$ corresponds to the midpoint between the ith and the $(i+k)$th site.

Notice that x_k can also be written in the form $x_k=(i\,s+k\,s/2)/(L_A s)$, where the lattice spacing now also occurs, and this form tells us that x_k becomes a function of the position $x\in A$ in the continuum limit. For a single block, the thermodynamic limits (7.15) have been studied in [13, 14] for free fermionic chains, also finding some analytic results, and in [15] for a harmonic chain, but in the latter case the corresponding analytic expressions are not available in the literature. In the case where A is the union of two disjoint blocks of a harmonic chain, the numerical results shown in figure 17 for $L_2=2L_1$ and in appendix C for $L_2=L_1$ (see figures 32 and 33) provide some evidence that the limits in (7.15) exist and that the functions $\tau_k(x_k)$ and $\nu_k(x_k)$ are not smooth. This feature prevents us from applying the continuum limit procedure described in [15] for the single block case in a straightforward way; indeed, in that analysis, the smoothness of the functions obtained from the thermodynamic limit of the diagonals is a crucial assumption. This lack of smoothness induces us to only consider the combinations of matrix elements providing the discrete approximations of the first derivatives of $\tau_k(x_k)$ and $\nu_k(x_k)$. Instead, we do not consider the combination of matrix elements of V corresponding to the discrete approximation of $\nu_k''(x)$, which occurs in the single block analysis of [15].

Following [15], let us introduce the following combinations of diagonals:

$$\mathsf{T}^{(0)}_{k_{\max}}(i)\equiv\begin{cases}T_{i,i}+2\displaystyle\sum_{k=1}^{k_{\max}}T_{i,i+k}\\[2ex] T_{i,i}+2\displaystyle\sum_{k=1}^{k_{\max}}T_{i-k,i}\end{cases}\qquad \mathsf{V}^{(0)}_{k_{\max}}(i)\equiv\begin{cases}V_{i,i}+2\displaystyle\sum_{k=1}^{k_{\max}}V_{i,i+k} & \quad\tilde{i}\in A_<\\[2ex] V_{i,i}+2\displaystyle\sum_{k=1}^{k_{\max}}V_{i-k,i} & \quad\tilde{i}\in A_>\end{cases}\tag{7.16}$$

https://doi.org/10.1088/1742-5468/addaa7

which include the main diagonals of T and V, respectively, and

$$\mathsf{V}^{(2)}_{k_{\max}}(i) \equiv \begin{cases} \displaystyle\sum_{k=1}^{k_{\max}} k^2\, V_{i,i+k} & \tilde{i} \in A_< \\ \displaystyle\sum_{k=1}^{k_{\max}} k^2\, V_{i-k,i} & \tilde{i} \in A_> \end{cases} \tag{7.17}$$

where the relation (2.18) between the matrix index $\tilde{i} \in [1, L_A]$ and the index i labelling the sites of the chain has been used and

$$\begin{aligned} A_< &\equiv [1\,, L_1/2] \cup [D + L_1 + 1\,, D + L_1 + L_2/2] \\ A_> &\equiv [L_1/2 + 1\,, L_1] \cup [D + L_1 + L_2/2 + 1\,, D + L_A] \end{aligned} \tag{7.18}$$

which are well defined for even values of L_1 and L_2. The branches $A_<$ and $A_>$ in (7.18) have been introduced by adapting the analysis for a single block [15] (where a symmetry with respect to the centre of the subsystem occurs) to this case. However, a different choice of $A_<$ and $A_>$ could provide better results. In particular, a definition of $A_<$ and $A_>$ based on x_χ seems natural, but we leave this analysis for future studies.

In this limiting procedure, the limit $L_A \to +\infty$ should be taken before the limit $k_{\max} \to +\infty$. In the numerical analysis, where both L_A and $k_{\max}$ are finite, this prescription corresponds to keeping $k_{\max} \ll L_A$. Considering $L_A \to +\infty$ first, from (7.16) and (7.17) one introduces

$$\mathcal{T}^{(0)}_{k_{\max}}(x) \equiv \lim_{L_A \to \infty} \frac{\mathsf{T}^{(0)}_{k_{\max}}(i)}{L_A} \qquad \mathcal{V}^{(0)}_{k_{\max}}(x) \equiv \lim_{L_A \to \infty} \frac{\mathsf{V}^{(0)}_{k_{\max}}(i)}{L_A} \qquad \mathcal{V}^{(2)}_{k_{\max}}(x) \equiv \lim_{L_A \to \infty} \frac{\mathsf{V}^{(2)}_{k_{\max}}(i)}{L_A} \tag{7.19}$$

where the RHSshs are functions of x; indeed, (7.15) can be employed to write them through the functions $\tau_k(x_k)$ and $\nu_k(x_k)$, which become functions of x in the continuum limit, as highlighted above (see the text below (7.15)). Then, taking $k_{\max} \to +\infty$ in (7.19) leads us to introduce, respectively,

$$\mathcal{T}^{(0)}_{\infty}(x) \equiv \lim_{k_{\max} \to \infty} \mathcal{T}^{(0)}_{k_{\max}}(x) \qquad \mathcal{V}^{(0)}_{\infty}(x) \equiv \lim_{k_{\max} \to \infty} \mathcal{V}^{(0)}_{k_{\max}}(x) \qquad \mathcal{V}^{(2)}_{\infty}(x) \equiv \lim_{k_{\max} \to \infty} \mathcal{V}^{(2)}_{k_{\max}}(x)\,. \tag{7.20}$$

Assuming that these functions are well defined, and also neglecting all the terms coming from the second and higher derivatives of $\tau_k(x_k)$ and $\nu_k(x_k)$ for the local term of the entanglement Hamiltonian in the continuum limit, we find

$$K_{A,\text{loc}} = \frac{\ell_A}{s^2} \int_A \frac{\mathcal{V}^{(0)}_{\infty}(x)}{2}\, \Phi(x)^2\, \mathrm{d}x + \ell_A \int_A \frac{1}{2} \left[\mathcal{T}^{(0)}_{\infty}(x)\, \Pi(x)^2 - \mathcal{V}^{(2)}_{\infty}(x) \left(\Phi'(x)\right)^2 \right] \mathrm{d}x + O(s)\,. \tag{7.21}$$

In figures 20 and 21, we numerically test the functions $\mathcal{T}^{(0)}_{\infty}(x)$, $\mathcal{V}^{(0)}_{\infty}(x)$ and $\mathcal{V}^{(2)}_{\infty}(x)$ introduced in (7.20) when $L_2 = 2L_1$ by reporting the numerical data obtained for the ratios $\mathsf{T}^{(0)}_{k_{\max}}(i)/L_A$, $\mathsf{V}^{(2)}_{k_{\max}}(i)/L_A$ and $\mathsf{V}^{(0)}_{k_{\max}}(i)$ (see (7.16) and (7.17)) with increasing values of L_A (see (7.19)) in the regime where $k_{\max} \ll L_A$, for various values of δ and $\omega L_A = 10^{-50}$. In appendix C, the same quantities have been considered for $L_2 = L_1$ (see figures 34 and 35) for $\omega L_A = 10^{-50}$. The black dashed curves in figures 20 and 34 denote the weight function (7.5), and its large separation distance limit corresponds to the solid green curves.

The values of $k_{\max}$ chosen in figures 20, 21, 34 and 35 correspond to the best collapses of the numerical data points among those that we have explored. In appendix C, considering the case of equal intervals, the crucial role of the parameter $k_{\max}$ is investigated by showing $\mathsf{T}^{(0)}_{k_{\max}}(i)/L_A$ and $\mathsf{V}^{(2)}_{k_{\max}}(i)/L_A$ for smaller and still non-trivial values of $k_{\max}$ (see figures 36 and 37).

In our numerical analyses, we have observed that less precision is needed in a massless regime with respect to the massive cases considered in section 6. Indeed, about 4000 digits have been employed when $L_2 \neq L_1$ in the massless regime, while about 5000 have been used to explore the large ω regime.

The collapses of the numerical data points in figures 21 and 35 suggest that the weight function for the $O(1/s^2)$ term in (7.21) vanishes identically, namely $\mathcal{V}^{(0)}_{\infty}(x) = 0$ (for the analogue of this result in the single interval case, see the left panel of figure 4 in [15]). Instead, the numerical results displayed in figures 20 and 34 tell us that a reasonable conjecture for the weight functions occurring in the $O(1)$ terms in (7.21) can be written through (7.5) as

$$\mathcal{T}^{(0)}_{\infty}(x) = \beta_{\text{loc}}(x) \qquad\qquad \mathcal{V}^{(2)}_{\infty}(x) = -\beta_{\text{loc}}(x)\,. \tag{7.22}$$

Following [12], an extrapolation of the numerical data has been performed in some cases. In particular, assuming $\mathsf{T}^{(0)}_{k_{\max}}(i) \approx \alpha_{\mathsf{T}} L_A + \beta_{\mathsf{T}}$ and $\mathsf{V}^{(2)}_{k_{\max}}(i) \approx \alpha_{\mathsf{V}} L_A + \beta_{\mathsf{V}}$ as $L_A \to \infty$, a fitting procedure has been employed to extract α_{T}, β_{T}, α_{V} and β_{V} from the data sets corresponding to large enough values of L_A. In the inset of the top panels in figures 20, 34, 36 and 37, the crosses correspond to α_{T} obtained through this extrapolation procedure, and good agreement is observed with (7.5). A similar analysis for α_{V} has been carried out only in the regions of A where the data points have a clear trend (*e.g.* in the bottom panels of figures 20 and 34, around the endpoints of the blocks), again finding agreement with (7.5).

In summary, while the numerical data points in the top panels of figures 20 and 34 support the conjecture for $\mathcal{T}^{(0)}_{\infty}(x)$ in (7.22), the numerical results displayed in the bottom panels of these figures are quite noisy, and therefore they do not provide convincing numerical evidence for the conjecture proposed in (7.22) for $\mathcal{V}^{(2)}_{\infty}(x)$.

Since the data points in figure 14 show the occurrence of the hyperbolic front (7.9), it is worth exploring the scaling of the elements in the off-diagonal blocks along this front. The results of this analysis are reported in appendix C. Here, we just mention that we find reasonable collapses of the data points when the elements of T along this front are divided by $\log L_A$, when both $L_1 = L_2$ and $L_1 \neq L_2$ (see the top panels in figures 38 and 39, respectively). In [28], a similar logarithmic scaling was observed in a free chiral current model (see section 8). Instead, for the matrix V, while a reasonable collapse of these elements is observed when $L_1 = L_2$ (see the bottom panel of figure 38), *i.e.* when

J. Stat. Mech. (2025) 073102

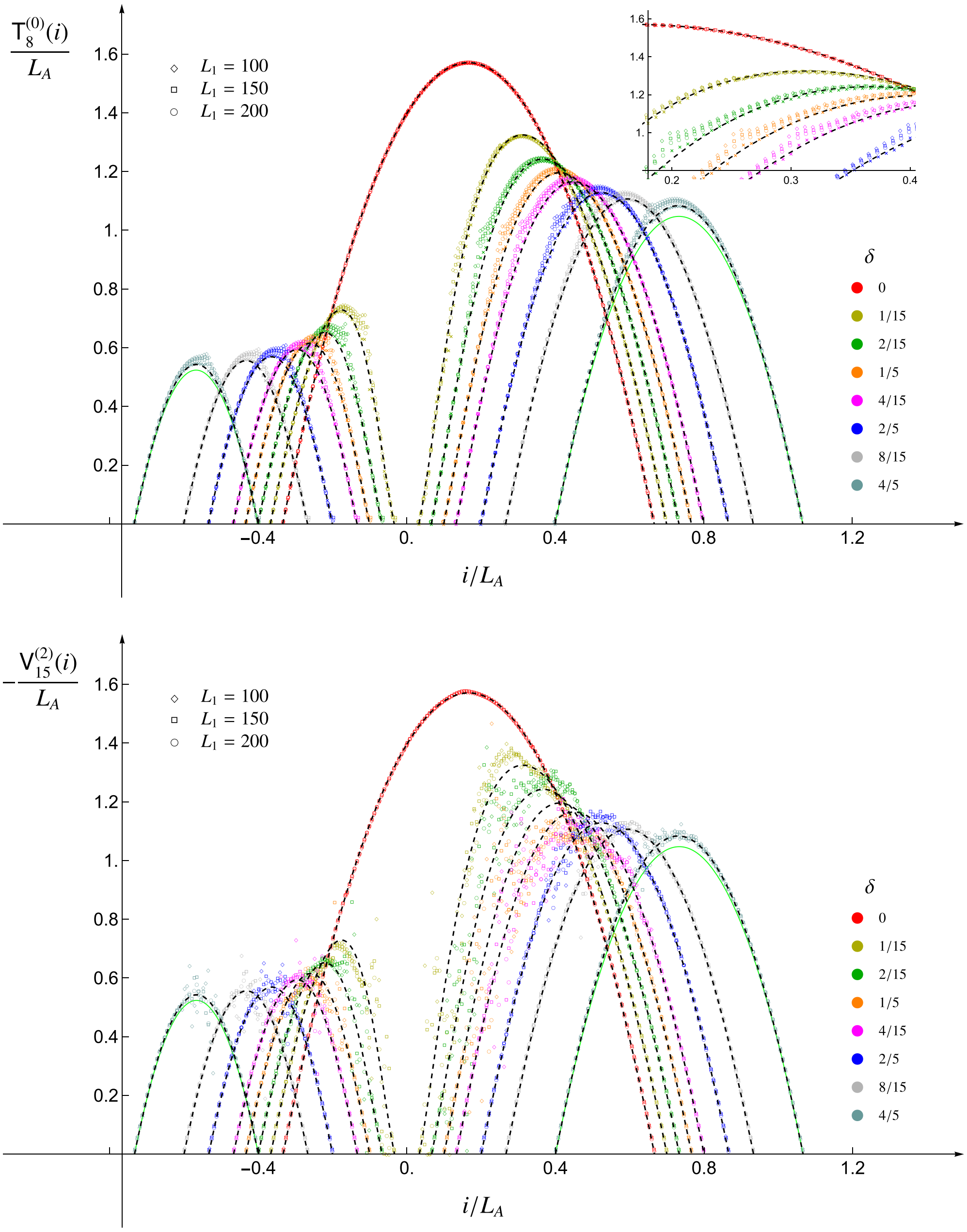

Figure 20. The combinations of diagonals defined in the first expression of (7.16) (top) and in (7.17) (bottom) for $k_{\max} \ll L_A$ (see also (7.19)) when $L_2 = 2L_1$. The dashed black curve corresponds to (7.5) and the solid green curve to its limit $d \to +\infty$ (see also figure 18).

the front (7.9) corresponds to the antidiagonal of V, it becomes unclear when $L_1 \neq L_2$ (see the bottom panel of figure 39).

Let us conclude our analysis of the entanglement Hamiltonians in a harmonic chain by remarking that, while regimes of large and vanishing ω have been explored quite extensively in the previous sections, the most important one, where the mass parameter

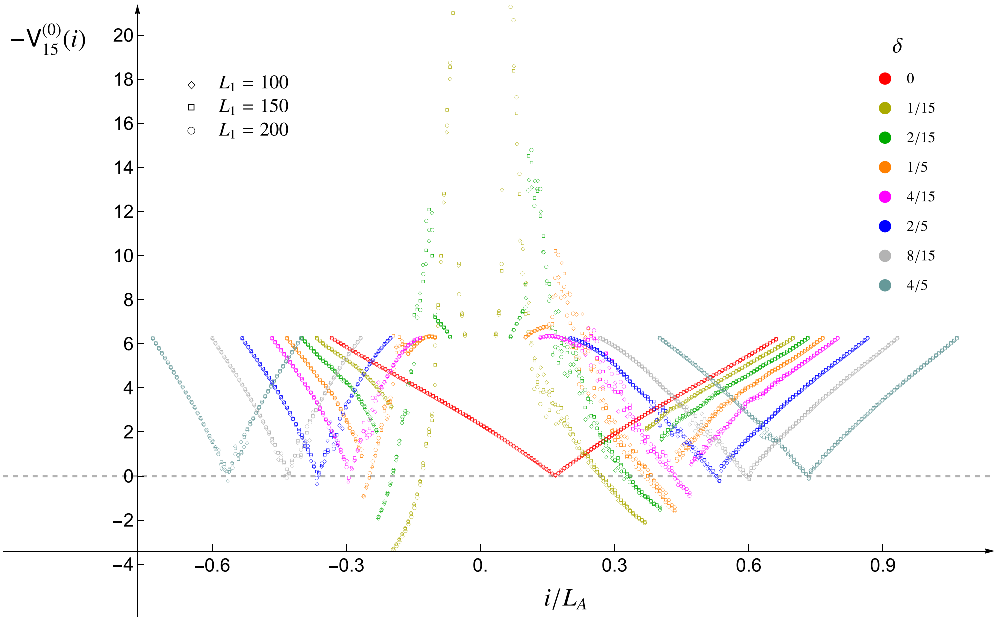

Figure 21. The combination of diagonals defined in the second expression of (7.16) for $k_{\max} \ll L_A$ (see also (7.19)) when $L_2 = 2L_1$.

takes finite and non-vanishing values, has been poorly discussed, except for the brief comments in section 3. This is because exploring this regime is very difficult. In order to gain insights about the entanglement Hamiltonian in this complicated regime, in appendix D we report the results of some numerical analyses for the case of a single block whose outcomes might provide some handle for exploring the continuum limit.

8. Free chiral current model

In this section, we explore the entanglement Hamiltonian of the union of two disjoint intervals $A = A_1 \cup A_2$ in the line for a free chiral current $j(x)$ given by the derivative of a massless scalar field, whose commutation relation is $\big[j(x), j(y)\big] = \mathrm{i}\,\delta'(x-y)$, when the entire system is in its ground state. This model has been explored *e.g.* in [28–30], and this quantity has been studied in [28], both in a continuum and in a lattice. In appendix E, the formulas for the entanglement entropies and the entanglement Hamiltonian in the lattice model of a chiral current [28] are reviewed. In appendix F, we discuss the Rényi mutual information for both a massless scalar and a chiral current.

The Hamiltonian of a lattice model on a circle made by L sites reads

$$\widehat{H} = \frac{1}{2}\sum_{i=1}^{L} \hat{b}_i^2 \,. \tag{8.1}$$

The operators $\hat{b}_i$ satisfy the commutation relations corresponding to the discretization of the commutation relation for a chiral current $j(x)$ in the continuum, namely

$$\left[\hat{b}_i\,,\hat{b}_j\right]=\mathrm{i}\,Y_{i,j}\qquad\qquad Y_{i,j}\equiv\delta_{j,i+1}-\delta_{j,i-1}\,.\tag{8.2}$$

Since periodic boundary conditions are imposed, matrix Y is non-invertible (indeed, its spectrum contains two vanishing eigenvalues).

The generic element of the correlation matrix is $B_{i,j}\equiv\langle\hat{b}_i\,\hat{b}_j\rangle$ for finite L when the system is in its ground state, which has been found in [28], and its limit $L\to+\infty$ reads

$$B_{i,j}=\begin{cases}-\dfrac{1+(-1)^{i-j}}{\pi\,(|j-i|^2-1)} & |j-i|\neq 1\\[2ex] \dfrac{\mathrm{i}}{2}\,Y_{i,j} & |j-i|=1\end{cases}\tag{8.3}$$

whose dependence on $|j-i|$ originates from the translational invariance of the model. We remark that the continuum limit of the lattice model described by (8.1) contains two free chiral currents [28, 30], as discussed in appendix E. This leads us to introduce a factor of 2 in a proper way in the process of comparing the lattice results against those in the continuum.

Considering the bipartition of the line characterized by subsystem A made by L_A sites (which are not necessarily contiguous), the crucial quantities related to the bipartite entanglement are obtained by restricting the correlation matrix (8.3) to A. In particular, in this way one obtains the $L_A\times L_A$ matrices Y_A and B_A from (8.2) and (8.3), respectively, which satisfy $\mathrm{Im}(B_A)=Y_A/2$. The matrix Y_A is invertible only for even values of L_A. Indeed, since Y_A is a real, antisymmetric and tridiagonal Toeplitz matrix, its eigenvalues are given by $\lambda_j=-2\,\mathrm{i}\cos[\pi\,j\,/(L_A+1)]$, which implies that Y_A is not invertible when L_A is odd; hence, only even values for L_A are considered in our analysis.

The technical details underlying the numerical evaluation of the entanglement entropies and the matrix characterizing the entanglement Hamiltonian from the matrices Y_A and B_A are reviewed in appendix E, following [28]. Some results about the Rényi mutual information of this model are discussed in appendix F.

In particular, by introducing the following $L_A\times L_A$ imaginary matrix

$$R_A\equiv-\mathrm{i}\,Y_A^{-1}B_A-\frac{1}{2}\,1=-\mathrm{i}\,Y_A^{-1}\,\mathrm{Re}\,(B_A)\tag{8.4}$$

where $\mathbf{1}$ is the $L_A\times L_A$ identity matrix, the entanglement Hamiltonian can be written as

$$\widehat{K}_A\equiv\hat{\boldsymbol{b}}^{\mathrm{t}}M\,\hat{\boldsymbol{b}}\qquad\qquad M\equiv-\frac{\mathrm{i}}{2}\,h\left(R_A^2\right)\,R_A\,Y_A^{-1}\tag{8.5}$$

in terms of the vector of operators given by $\hat{\boldsymbol{b}}^{\mathrm{t}}=\left(\hat{b}_1,\dots,\hat{b}_{L_A}\right)$ and of the function $h(y)$ defined in (2.13).

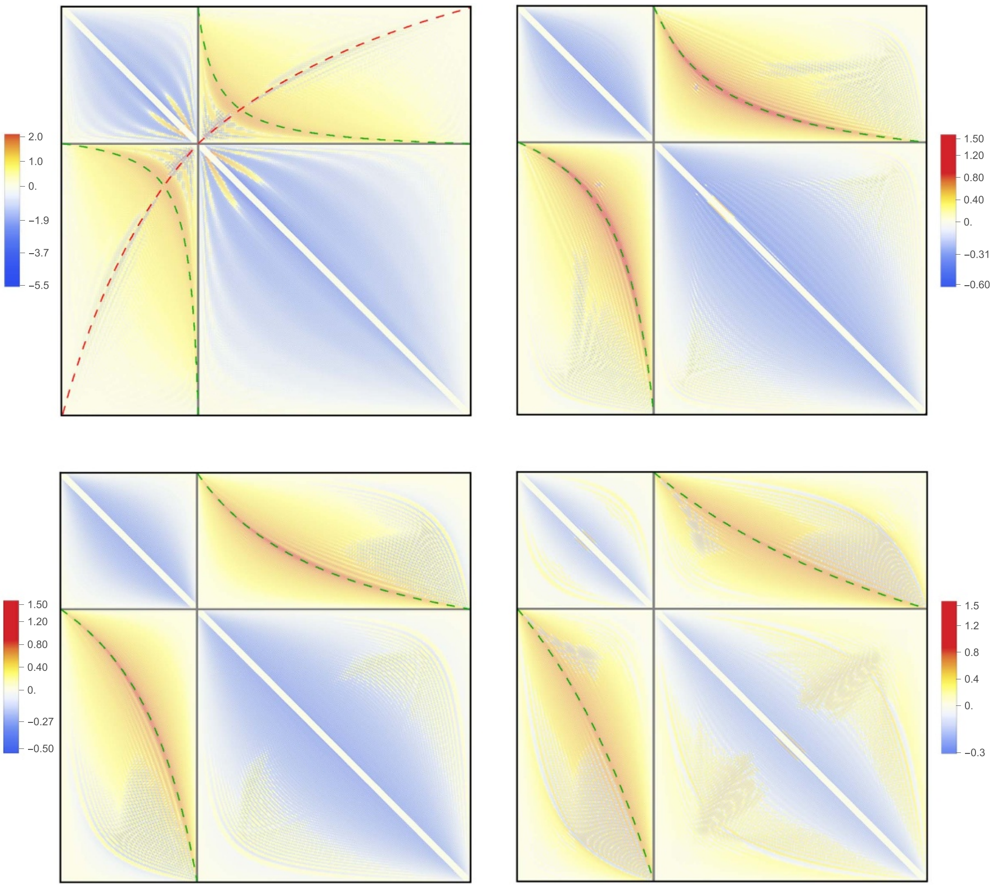

Figure 22. Matrix M in (8.5) for $L_2 = 2L_1$ with $L_1 = 150$ and the separation distance given by $\delta = 1/15$ (top left), $\delta = 4/15$ (top right), $\delta = 8/15$ (bottom left) and $\delta = 3/2$ (bottom right).

Since we consider the case where the subsystem $A = A_1 \cup A_2$ is made by two disjoint blocks, the real and symmetric $L_A \times L_A$ matrix M in (8.5) is naturally decomposed as follows:

$$M = \left(\begin{array}{c|c} M^{(1,1)} & M^{(1,2)} \\ \hline M^{(2,1)} & M^{(2,2)} \end{array}\right) \tag{8.6}$$

where the diagonal blocks $M^{(1,1)}$ and $M^{(2,2)}$ correspond to A_1 and A_2 , respectively; hence, they are $L_1 \times L_1$ and $L_2 \times L_2$ symmetric matrices, respectively.

In figure 22, we show matrix M in (8.5) for $L_2 = 2L_1$ with $L_1 = 120$ and various separation distances, identifying the blocks occurring in the decomposition (8.6) through grey segments. The main diagonal and the other two diagonals next to it in both directions (hence five diagonals in total), which contain the elements with large amplitudes, have been removed in order to make visible the remaining non-vanishing elements. The green and red dashed lines correspond to x_c and x_Γ in (7.7) and (7.9), respectively, like in figure 14.

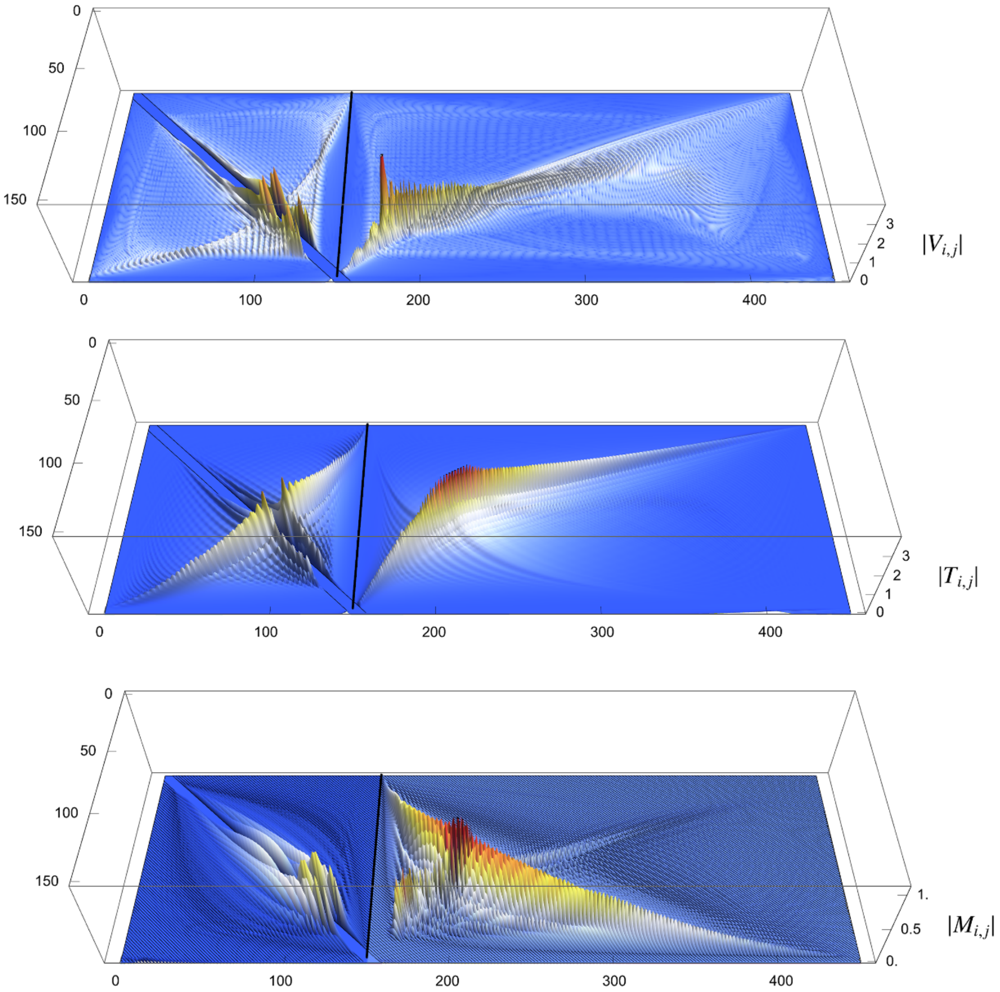

Figure 23. Matrix elements $|T_{i,j}|$ (top), $|V_{i,j}|$ (middle) and $|M_{i,j}|$ (bottom) with $i \in A_1 \cup A_2$ and $j \in A_1$ (see (3.1) and (8.6)) for $L_2 = 2L_1$ with $L_1 = 150$ and the separation distance given by $\delta = 2/15$. The data in the top and middle panels are obtained for $\omega = 10^{-500}$. While the front corresponding to x_χ (see (7.10)) is visible in the diagonal block of T and V (top and middle panels), it does not occur in the diagonal block of M (bottom panel).

Comparing the matrix M in figure 22 for the chiral current with the matrices T and V in figure 14 for the massless scalar, the most relevant feature to highlight is the absence of the front given by x_χ (see (7.10)) in the diagonal blocks of M, which occurs in the diagonal blocks of T and V instead (see the dashed black curves in figure 14). A comparison among matrices T, V and M has also been performed in figure 23 by considering the absolute value of their elements and showing a three-dimensional representation of their upper blocks (see (3.1) and (8.6)) for $L_2 = 2L_1$, $L_1 = 150$ and $\delta = 2/15$ (the largest diagonals have been removed, as was done in figure 14 and in figure 22). One also realizes from figure 23 that the front for x_χ (see (7.10)) does

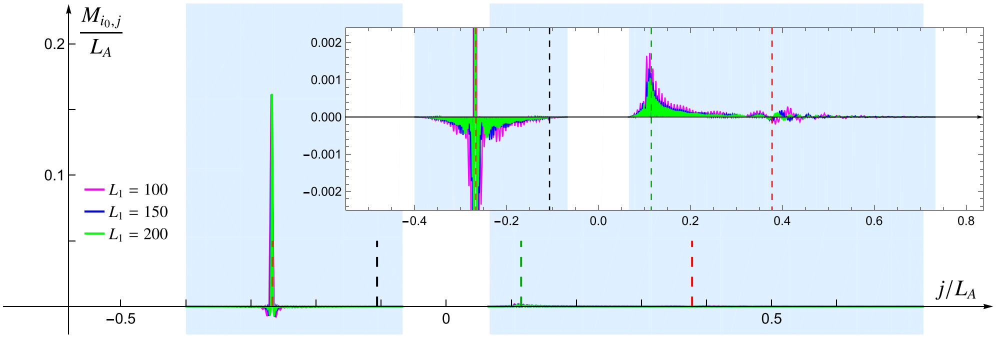

Figure 24. Matrix elements of M along the row labelled by $i = i_0$. Here, $L_2 = 2L_1$, $\delta = 2/15$ and $i_0 = \frac{2}{5}L_1$. The green, red, black and brown vertical dashed segments denote the intersections of the row with (7.7), (7.9), (7.10) and the main diagonal, respectively (see also the dashed lines in figures 14 and 22).

not occur in the diagonal block in the bottom panel, while it is clearly visible in the other two diagonal blocks, as already remarked above.

We remark that the diagonal blocks $M^{(1,1)}$ and $M^{(2,2)}$ (see (8.6)) in figure 22 display the same qualitative structure observed from the analytic expression, as shown in figure 5 of [28].

In figure 24, we display some numerical data for the matrix elements $M_{i_0,j}/L_A$ along the line labelled by $i = i_0$, for $L_2 = 2L_1$, $\delta = 2/15$, $i_0 = \frac{2}{5}L_1$ and various values of L_1. The dashed vertical lines denote the intersections of the row with x_c, x_Γ, x_χ (see (7.7), (7.9) and (7.10), respectively) and the main diagonal, like in figure 15. From the inset of figure 24, we observe that the amplitude of the matrix elements increases around the intersection with the main diagonal, x_c and x_Γ, but a significant change in the amplitude does not occur around x_χ, like in the fermionic case discussed in appendix B (see figure 30). It is worth comparing figure 24 with figure 15, in order to appreciate the qualitative differences in these profiles.

It is instructive to consider the single-particle entanglement spectrum of the entanglement Hamiltonian for the chiral current that we are exploring and to compare the result with the corresponding one for a harmonic chain in a massless regime (see figure 16). This comparison has been performed in figure 25, for configurations with $L_2 = 2L_1$. Taking into account the doubling in the proper way (see the caption of the figure), a good match of the data points is observed between these two quantities. Since the two underlying models are not equivalent [28, 30], it would be insightful to understand this numerical agreement analytically.

Another instructive comparison between the massless harmonic chain and the lattice model for the chiral current is based on the mutual information and its generalization given by the Rényi mutual information, which involves the Rényi entropies, whose continuum limit has been explored in [28, 35], finding analytic results. We remark that, in the continuum limit, these two bosonic lattice models are different. Indeed, for instance, the massless scalar satisfies the Haag duality, while the chiral current does not

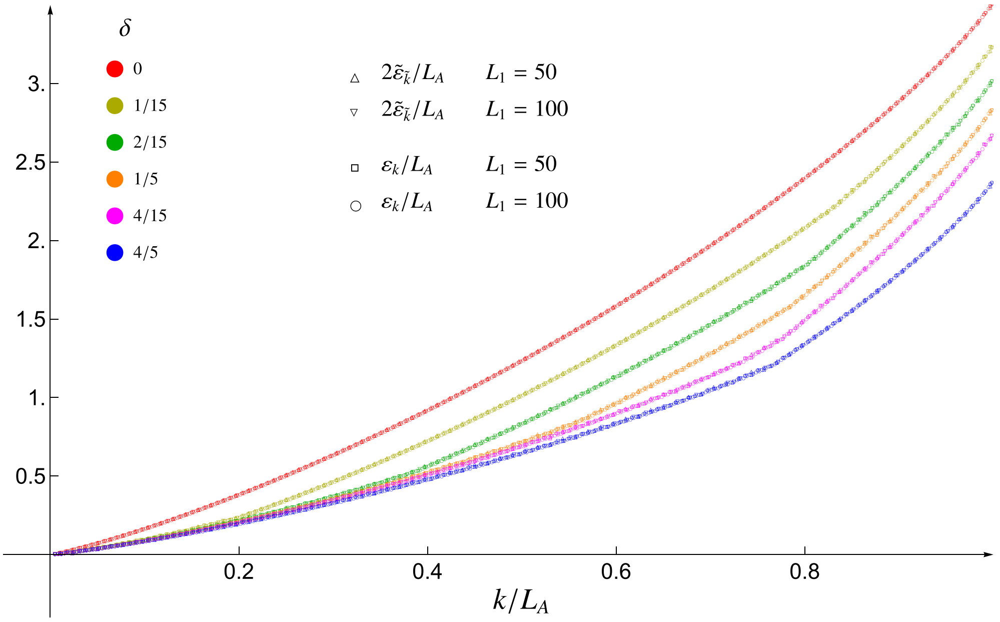

Figure 25. Single-particle entanglement spectrum $\tilde{\varepsilon}_{\tilde{k}}$ for a chiral current and single-particle entanglement spectrum ε_k for a massless ($\omega = 10^{-50}$), when A is made by two blocks $L_2 = 2L_1$ (see also the bottom panel of figure 16, where the data points for ε_k in this setup are also displayed). The relation $\tilde{k} = k/2$ has been used in the comparison of these two single-particle entanglement spectra.

possess this property [28]. The comparison between the Rényi mutual information in these models is discussed in appendix F, where we also provide some numerical checks of the analytic expressions through lattice computations (see figures 43 and 44).

In figure 26, we display some numerical data for the main diagonal $M_{i,i}$ and the first non-vanishing diagonal $M_{i,i+2}$ of matrix M defined in (8.5). Indeed, all the odd diagonals of M vanish, namely $M_{i,i+2k+1} = 0$ for $k \geqslant 0$. This feature agrees with the fact that this model exhibits a parity symmetry (see $\hat{b}_i \to (-1)^i\, \hat{b}_i$ in appendix E) [30], which also implies that $B_{i,i+2k+1} = 0$ in (8.3). Notice that, instead, all the diagonals of matrices T and V explored in section 7 are typically non-vanishing. The collapses of the data points in the left panels of figure 26 indicate that $M_{i,i}/L_A$ and $M_{i,i+2}/L_A$ provide well-defined continuous functions as $L_A \to +\infty$. However, the corresponding right panels show that these continuous functions are not smooth because their second derivative is discontinuous. This lack of smoothness has also been observed for matrices T and V (see the right panels of figure 17).

It is worth adapting the analysis performed in section 7 for a massless harmonic chain to a chiral current model. This leads us to consider the sum of all the elements of a block of M along a row. In particular, in the diagonal and off-diagonal blocks of M (see (8.6)), let us introduce, respectively,

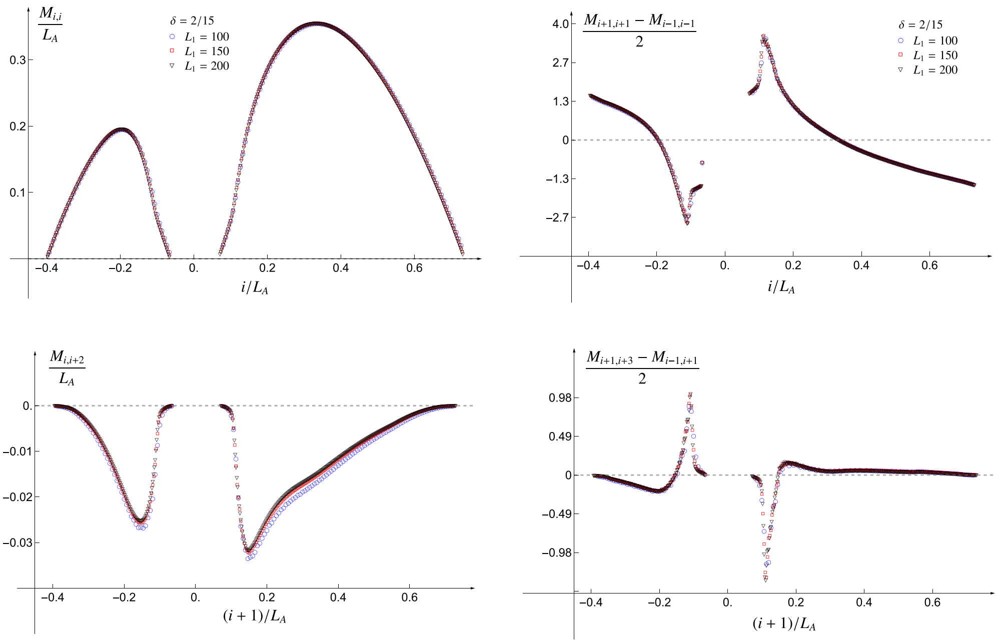

Figure 26. Diagonals $M_{i,i}$ (top left) and $M_{i,i+2}$ (bottom left) and their discrete first derivative in the corresponding right panels for $L_2 = 2L_1$.

$$\mathsf{M}_{\text{diag}}(i) = \sum_{j\in A_n} M_{i,j}^{(n,n)} \qquad i \in A_n \tag{8.7}$$

$$\mathsf{M}_{\text{off}}(i) = \sum_{j\in A_n} M_{i,j}^{(m,n)} \qquad i \in A_m \qquad m \neq n\,. \tag{8.8}$$

Some numerical results for these quantities are reported in figure 27, and the perfect collapses of the data points for increasing values of L_1 indicate that the ratios $\mathsf{M}_{\text{diag}}(i)/L_A$ and $\mathsf{M}_{\text{off}}(i)/L_A$ provide well-defined functions in the thermodynamical limit $L_A \to +\infty$ for a given value of L_2/L_1. The results of the corresponding analyses for matrices T and V are reported in figures 18 and 19. The dashed black curves correspond to $\beta_{\text{loc}}(x)/4$, from (7.5), and the solid green curves to its limit as the large separation distance diverges.

By comparing the numerical results for the row-wise summations (8.7) and (8.8) displayed in figure 27 with the corresponding ones for the row-wise summations of matrix T in (7.13), reported in figure 18, a remarkable qualitative similarity is observed.

It is also worth adapting the procedure discussed in section 7 for a massless harmonic chain to the chiral current model that we are exploring. Thus, in analogy with (7.16), let us introduce

https://doi.org/10.1088/1742-5468/addaa7

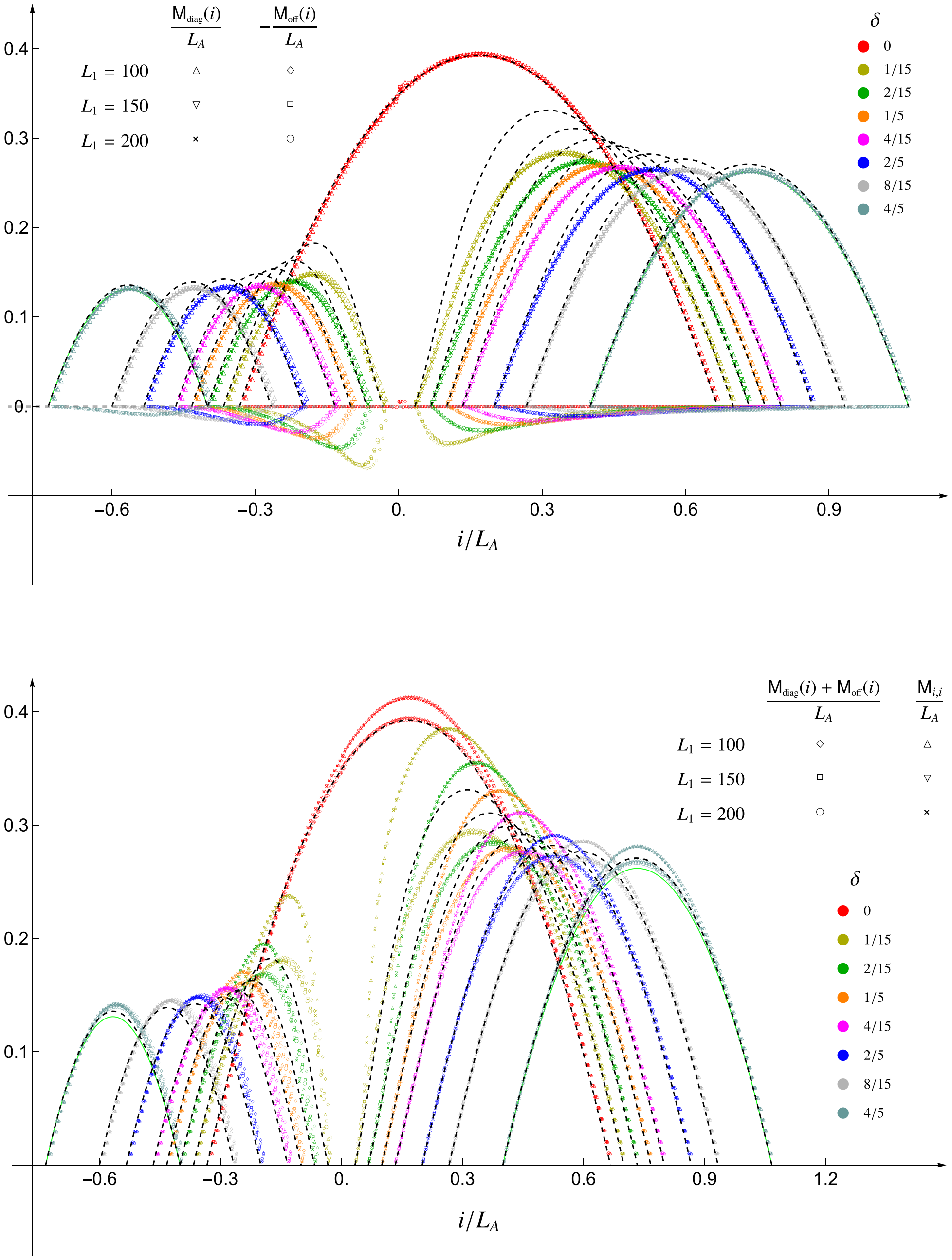

Figure 27. Combinations of elements in M introduced in (8.7) and (8.8) for $L_2 = 2L_1$.

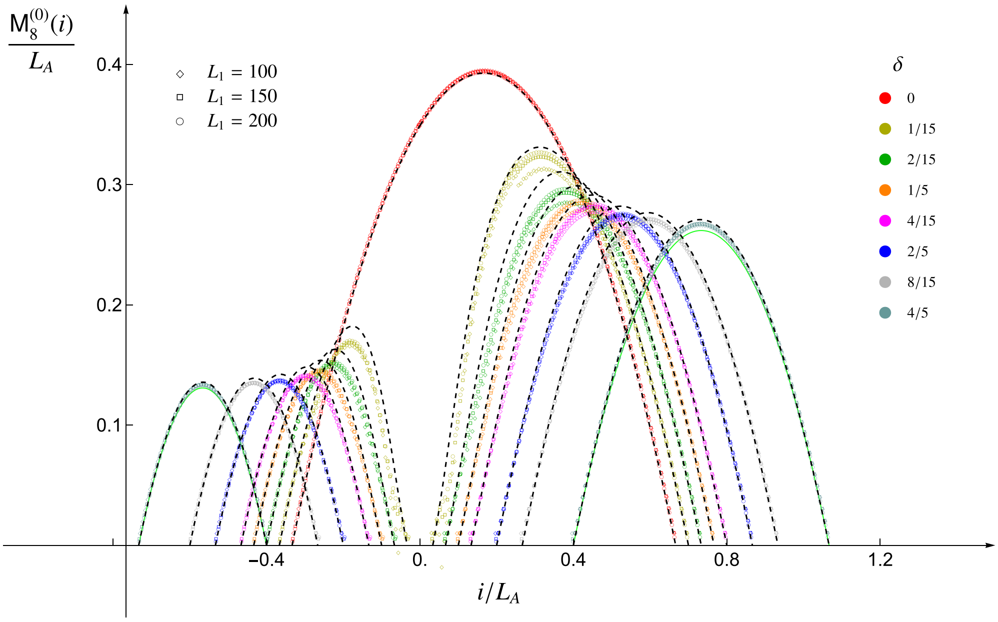

Figure 28. The combinations of diagonals in (8.9) for an optimal $k_{\max} \ll L_A$ when $L_2 = 2L_1$.

$$\mathsf{M}^{(0)}_{k_{\max}}(i) \equiv \begin{cases} M_{i,i} + 2\sum_{k=1}^{k_{\max}} M_{i,i+k} & \tilde{i} \in A_< \\ M_{i,i} + 2\sum_{k=1}^{k_{\max}} M_{i-k,i} & \tilde{i} \in A_> \end{cases} \tag{8.9}$$

where $A_<$ and $A_>$ are defined in (7.18); hence, only the elements in the diagonal blocks of M occur. In figure 28, some numerical results for (8.9) are shown, and they are compared against the same dashed black and solid green curves occurring in figure 27. The value of $k_{\max} \ll L_A$ has been chosen in the optimal way, in order to have stable curves. Comparing figure 28 with the top panel of figure 20 for matrix T, a remarkable similarity is observed.

The discrepancy occurring in both figures 27 and 28 between the curves defined by the data points and the dashed black curves could be understood by properly taking into account the non-local terms in the entanglement Hamiltonian found in [28].

9. Conclusions

In this paper, we have reported some numerical analyses for the entanglement Hamiltonian of the union of two disjoint blocks $A = A_1 \cup A_2$ in an infinite harmonic chain in its ground state (section 2). Our main results are obtained in the two limiting regimes of large mass (sections 5 and 6) and vanishing mass (sections 7 and 8). Some observations have also been made in the crossover regime where the mass parameter takes finite and non-vanishing values (section 3 and appendix D). Since this entanglement Hamiltonian has a quadratic form (2.10), it is characterized by the $L_A \times L_A$ real and symmetric matrices T and V, where L_A is the size of the subsystem, namely $L_A = L_1 + L_2$ for two disjoint blocks, where L_j is the number of sites in the block A_j.

In a large mass regime (sections 5 and 6), we have extended the analysis of the entanglement Hamiltonian of the single block reported in [21] to the case of two disjoint blocks. For this configuration, matrices T and V also become tridiagonal in this regime; hence, they are fully described by the profiles of the diagonals whose elements are $T_{i,i}$, $V_{i,i}$ and $V_{i,i+1}$. We observe that the analytic expressions for these profiles are described by (5.1) and (5.2) when $L_1 = L_2$ and by (6.1) and (6.2) when $L_1 < L_2$, in terms of piecewise linear functions whose slopes are written explicitly in terms of the analytic result for the entanglement Hamiltonian of a half chain found in [7] (see section 4). These piecewise linear functions can be discontinuous, and their disconnected terms are represented pictorially in figure 3 for $L_1 = L_2$ and in figure 6 for $L_1 < L_2$. Remarkable agreement with the numerical data points is observed, as shown in figure 4 when $L_1 = L_2$ and in figures 8 and 9 when $L_1 < L_2$. The main feature to highlight about the large mass regime is the occurrence of sharp transitions in the profiles of the diagonals as the dimensionless parameter $\delta \equiv D/L_A$ changes, with D being the number of sites separating the two blocks. Furthermore, we have observed two qualitatively different behaviours depending on the value of the dimensionless ratio $\rho \equiv L_1/L_A$ characterizing the relative size of the two blocks, introduced in (2.16), whose critical value corresponds to $L_2 = 3L_1$ (see (6.5)) (see figure 7 for a pictorial representation). We remark that the mutual information does not display these transitions; indeed, the area law holds in this regime. Instead, sharp transitions corresponding to the same critical values observed for the entanglement Hamiltonian occur in the single-particle entanglement spectrum. This quantity is well described by continuous piecewise linear functions given in (5.13) and (6.21) for $L_1 = L_2$ and $L_1 < L_2$, respectively. Also for the entanglement spectra, good agreement with the numerical data points has been found, as shown in figure 5 for $L_1 = L_2$ and in figures 10 and 11 for $L_1 < L_2$. A heuristic picture explaining the critical values of δ observed in our numerical analyses is described in section 6.3.

In a regime of vanishing mass, both a harmonic chain in a massless limit [3] and a free chiral current [28] have been explored, in sections 7 and 8, respectively. While in a harmonic chain the entanglement Hamiltonian is characterized by the pair of $L_A \times L_A$ matrices T and V discussed above, in a free chiral current model, it is fully described by the $L_A \times L_A$ matrix M given in (8.5). All these matrices display inhomogeneities and long-range couplings (see figures 14, 22 and 23). Besides the largest contributions to the entanglement Hamiltonian given by the elements around the main diagonal of these matrices, the subleading contributions are observed along specific fronts described by the analytic expressions in (7.7), (7.9) and (7.10) (see the dashed curves in figures 14 and 22 and also the vertical dashed lines in figures 15 and 24). We remark that the fronts corresponding to (7.10) in the diagonal blocks are not observed for a chiral current, and this provides an interesting qualitative difference between the two models that would be worth explaining in future studies.

The thermodynamic limit of the main contributions to the entanglement Hamiltonian, which are given by the main diagonal and the nearby diagonals of the matrices mentioned above, have been explored (see figure 17 for a harmonic chain and figure 26 for a chiral current), as was done in [13, 15] for a single block in infinite chains, finding continuous curves with a discontinuous second derivative. The latter feature has not been observed in the case of a single block. It would be insightful to obtain analytic expressions for these non-smooth curves, as was done in [13] for a single block in an infinite fermionic hopping chain.

Following the numerical analyses reported in [12, 23] to recover the weight functions in the entanglement Hamiltonians of two disjoint blocks on the line in the continuum limit, we have considered the summations of the matrix elements along a given row (see (7.13), (7.14) and (8.7), (8.8)) and also some specific combinations of diagonals (see (7.16), (7.17) and (8.9)). Remarkable collapses of the numerical data points are observed for these row-wise summations, as shown in figures 18 and 19 for a harmonic chain and in figure 27 for a chiral current. Instead, for the combinations of diagonals, the collapses are less clean (see figures 20 and 21 for a harmonic chain and figure 28 for a chiral current). These results should be compared against analytic expressions of the weight functions occurring in the entanglement Hamiltonian of two disjoint intervals in the continuum limit, which are available in the literature for a chiral current [28] but are still unknown for a massless scalar. The entanglement Hamiltonian of two disjoint intervals is non-local in both these models, and it worth exploring a possible relation between these non-local operators. While for a chiral current a fully non-local expression has been proposed [28], for a massless scalar we cannot establish whether this quadratic operator is fully non-local as well or just bi-local, like for a massless Dirac field [22].

The single-particle entanglement spectra for two disjoint blocks in these two infinite bosonic chains have also been investigated, finding the numerical results reported in figure 16 for a harmonic chain and in figure 25 for a chiral current. Furthermore, in figure 25 it has also been shown that a simple relation occurs between these two single-particle entanglement spectra. Explaining such numerical agreement would gain relevant insights into the comprehension of the relation between a harmonic chain and a chiral current model.

Analytic results for the continuum limit are available for the mutual Rényi information, both in a harmonic chain in a massless regime [35] and in a chiral current model [28]. Further numerical checks of these analytic expressions are reported in appendix F (see figures 43 and 44).

In a regime where the mass parameter is neither very large nor vanishing, some numerical results about the entanglement Hamiltonians in a harmonic chain have been reported, both for a single block (appendix D) and for two disjoint blocks (section 3). In the latter case, in comparison with a large mass regime, we observe that the three-diagonals approximation does not hold (see figure 1) and also the sharp transitions do not occur anymore (see figure 2). For a single block, the limiting procedure employed in [15] for a massless regime has been considered (see figure 40) and also alternative procedures have been proposed, which display better data collapses (see figures 41 and 42). Although these results provide some interesting insights for the continuum limit, they do not provide a prediction for the entanglement Hamiltonian of a single interval for a massive scalar field. This operator is fully non-local, and finding its explicit expression is still an important open problem.

The results presented in this article suggest some interesting questions. For instance, in a large mass regime, since the mutual information does not capture the sharp transitions observed in the entanglement Hamiltonian and in the single-particle entanglement spectrum, it would be interesting to find some simpler entanglement quantifier that can detect this feature of the large mass regime. We find it is also worth trying to extend the analysis recently described in [57] for a single block to the case of two disjoint blocks, in order to see whether the piecewise linear profiles that we have obtained also occur through this approach.

Our analyses can be extended in various directions. First, the quantities and various regimes that we have discussed for a harmonic chain should also be explored in some fermionic chains (see *e.g.* [66] for an interacting case). Furthermore, one could consider the possibility of exploring entanglement Hamiltonians for an arbitrary number of disjoint blocks [22], in systems with boundaries [23, 24, 67, 68] or with point-like defects [25], in inhomogeneous systems [69–71] and in time-dependent scenarios, such as, for example, those provided by quantum quenches [11, 56, 72–75]. We find it would also be worth investigating the entanglement spectra associated with these entanglement Hamiltonians [11, 76, 77] and extending all these questions to models in higher dimensions [16, 78, 79] or to other non-relativistic quantum systems [80–83].

Acknowledgments

We are grateful to Giuseppe Di Giulio for collaboration at the initial stage of this project. It is our pleasure to thank Jérôme Dubail, Mihail Mintchev, Christoph Minz, Diego Pontello and especially Viktor Eisler and Ingo Peschel for useful discussions or correspondence.

Appendix A. Large ω regime: an equivalent description of the diagonals

In this appendix, we provide the definition of $F_2(\delta,\rho;x)$ to employ in (6.1) and (6.2) for the parameterized endpoints of $A = A_1 \cup A_2$ given in (6.14). The result is obtained by adapting the procedure described in section 6.1, where the parameterized (6.13) is chosen and therefore (6.17) and (6.18) must be employed.

Setting the origin O in the second endpoint of A_1, in order to fix the parameters in the auxiliary functions (6.6)–(6.12), here we consider the rhombus $\mathcal{R}_0$ with vertices in O, P_0 and $P_\pm$, where

$$P_0 \equiv (0\,,\rho) \qquad\qquad P_- \equiv (-\rho/2\,,\rho/2) \qquad\qquad P_+ \equiv (3\rho/2\,,\rho/2) \tag{A.1}$$

hence the edges of $\mathcal{R}_0$ have slopes ±1 and ±1/3. The other rhombus $\widetilde{\mathcal{R}}$ to consider has vertices in P_0, P_+, $Q_<$ and $Q_>$, where

$$Q_< \equiv (1-2\rho\,,1/2) \qquad\qquad Q_> \equiv \left(\frac{2-\rho}{2}\,,\frac{1-\rho}{2}\right) \tag{A.2}$$

implying that its edges have slopes ±1/2 and ±1/3 for any value of ρ. In the limiting case of equal blocks, *i.e.* when $\rho = 1/2$, we have $Q_< = P_0$ and $Q_> = P_+$; hence, only $\mathcal{R}_0$ occurs also for this parameterized of the endpoints of A.

The parameters in the auxiliary functions (6.6)–(6.12) occurring in the definition of $F_2(\delta,\rho;x)$ for the four phases I, II, III and IV are determined from the rhombi $\mathcal{R}_0$ and $\widetilde{\mathcal{R}}$ introduced above, according to the same principle adopted in section 6.1 (see figure 7). This analysis allows us to construct the function $F_2(\delta,\rho;x)$ corresponding to the parameterized (6.14) for A.

When $\rho \in \big(0, \rho_{\rm c}\big]$, we find

$$F_2(\delta,\rho;x) \equiv \begin{cases} \Delta_1(x) + \Delta_2(x) & \delta \in \big[\,\delta_{\rm c}^{\rm I/II}, +\infty\big) \\ \Delta_1(x) + \bar{\Delta}_2(2a_2 - \rho/2; x) & \delta \in \big[\,\delta_{\rm c}^{\rm II/III}, \delta_{\rm c}^{\rm I/II}\big] \\ \Delta_1(x) + \tilde{\Delta}_2(2a_2 - \rho/2, 2a_2; x) & \delta \in \big[\,\delta_{\rm c}^{\rm III/IV}, \delta_{\rm c}^{\rm II/III}\big] \\ \lambda_1(-a_2/2; x) + \tilde{\lambda}_2(3a_2/2, \rho - a_2, 2a_2; x) & \delta \in \big[\,0, \delta_{\rm c}^{\rm III/IV}\big] \end{cases} \tag{A.3}$$

while for $\rho \in \big[\rho_{\rm c}, 1/2\big]$ the function $F_2(\delta,\rho;x)$ is

$$F_2(\delta,\rho;x) \equiv \begin{cases} \Delta_1(x) + \Delta_2(x) & \delta \in \big[\,\delta_{\rm c}^{\rm I/II}, +\infty\big) \\ \Delta_1(x) + \bar{\Delta}_2(2a_2 - \rho/2; x) & \delta \in \big[\,\delta_{\rm c}^{\rm II/III}, \delta_{\rm c}^{\rm I/II}\big] \\ \lambda_1(-a_2/2; x) + \bar{\lambda}_2(3a_2/2, \rho - a_2; x) & \delta \in \big[\,\delta_{\rm c}^{\rm III/IV}, \delta_{\rm c}^{\rm II/III}\big] \\ \lambda_1(-a_2/2; x) + \tilde{\lambda}_2(3a_2/2, \rho - a_2, 2a_2; x) & \delta \in \big[\,0, \delta_{\rm c}^{\rm III/IV}\big]\,. \end{cases} \tag{A.4}$$

This function satisfies the consistency conditions (6.19) and (6.20) in the limiting regimes of vanishing and large separation distances, as already mentioned in the main text just below these requirements.

Appendix B. Entanglement Hamiltonian in an infinite fermionic chain

In order to make a comparison with the bosonic lattice models discussed in the main text, in this appendix we consider the entanglement Hamiltonian of two disjoint blocks in an infinite fermionic hopping chain and review the formulas underlying the numerical analysis of its continuum limit [23], which provides the entanglement Hamiltonian of two disjoint intervals for a massless Dirac field on the line and in its ground state, found in [22].

The free massless Dirac field is a prototypical example of two-dimensional CFT with central charge $c = 1$. This fermionic field is a doublet made by two chiral complex fields, in terms of the light-cone coordinates $u_\pm \equiv x \pm t$. In the case where this model is defined on the line and in its ground state, the entanglement Hamiltonian of subsystem A given by the union of two disjoint intervals ($i.e.$ $A \equiv A_1 \cup A_2$, where $A_j \equiv [a_j, b_j]$ with $j \in \{1,2\}$) is the sum of a local term and a bi-local term [22]:

$$K_A = K_{A,\text{loc}} + K_{A,\text{biloc}}\,. \tag{B.1}$$

The local term is

$$K_{A,\mathrm{loc}} = \int_A \beta_{\mathrm{loc}}(x)\, T_{tt}(x)\, \mathrm{d}x \tag{B.2}$$

where the weight function $\beta_{\mathrm{loc}}(x)$ has been introduced in (7.5), and $T_{tt}(x)$ is the energy density of the massless Dirac field, namely

$$T_{tt}(x) \equiv \frac{\mathrm{i}}{2}\Big[\Big(:\psi^*_{\mathrm{R}}\,(\partial_x\psi_{\mathrm{R}}): - :\Big(\partial_x\psi^*_{\mathrm{R}}\Big)\,\psi_{\mathrm{R}}:\Big)(x) - \Big(:\psi^*_{\mathrm{L}}\,(\partial_x\psi_{\mathrm{L}}): - :\Big(\partial_x\psi^*_{\mathrm{L}}\Big)\,\psi_{\mathrm{L}}:\Big)(x)\Big] \tag{B.3}$$

where ψ_{R} and ψ_{L} are the right and left chiral components of the massless Dirac field. The bi-local term is

$$K_{A,\mathrm{biloc}} = \int_A \beta_{\mathrm{biloc}}(x)\, T_{\mathrm{biloc}}(x, x_{\mathrm{c}})\, \mathrm{d}x \tag{B.4}$$

whose weight function can be written through (7.5) and the conjugate point (7.7), as follows:

$$\beta_{\mathrm{biloc}}(x) = \frac{\beta_{\mathrm{loc}}(x_{\mathrm{c}})}{x - x_{\mathrm{c}}} \tag{B.5}$$

and the bi-local quadratic operator $T_{\mathrm{biloc}}(x,y)$ is defined as

$$T_{\mathrm{biloc}}(x,y) \equiv \frac{\mathrm{i}}{2}\Big[:\Big(\psi^*_{\mathrm{R}}(x)\,\psi_{\mathrm{R}}(y) - \psi^*_{\mathrm{R}}(y)\,\psi_{\mathrm{R}}(x)\Big): - :\Big(\psi^*_{\mathrm{L}}(x)\,\psi_{\mathrm{L}}(y) - \psi^*_{\mathrm{L}}(y)\,\psi_{\mathrm{L}}(x)\Big):\Big]. \tag{B.6}$$

The operator (B.1) can be obtained from a lattice model through a continuum limit.

Consider an infinite fermionic hopping chain characterized by the following Hamiltonian:

$$\widehat{H} = -\frac{1}{2}\sum_{i\,\in\mathbb{Z}}\Big(c^\dagger_i c_{i+1} + c^\dagger_{i+1} c_i\Big) + \mu \sum_{i\,\in\mathbb{Z}} c^\dagger_i c_i \tag{B.7}$$

in terms of the fermionic creation and annihilation operators and of the chemical potential $\mu = \cos q_{\mathrm{F}}$, whose ground state is a Fermi sea with occupied momenta $q \in [-q_{\mathrm{F}}, q_{\mathrm{F}}]$. The generic element of the correlation matrix is

$$C_{i,j} \equiv \langle c^\dagger_i c_j\rangle = \frac{\sin[q_{\mathrm{F}}\,(i-j)]}{\pi\,(i-j)} \tag{B.8}$$

and its restriction to subsystem A defines the reduced correlation matrix C_A, which is the crucial quantity to explore in order to study the bipartite entanglement in this setup.

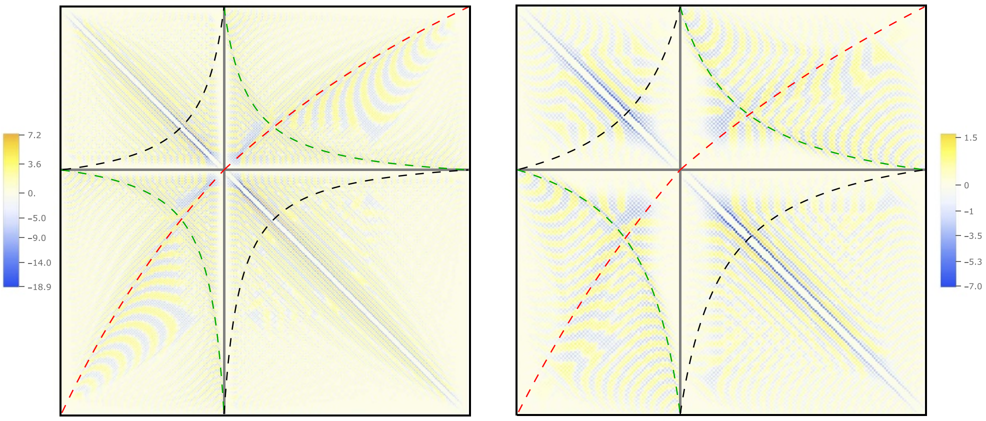

Figure 29. Matrix H for $L_2 = 1.5L_1$ with $L_1 = 120$ and $\delta = 1/10$ (left) or $\delta = 1/4$ (right).

We are interested in a free fermionic chain ([B.7]) in its ground state when the bipartition of the infinite chain is given by the union of two disjoint blocks $A = A_1 \cup A_2$, made by L_1 and L_2 contiguous sites. The entanglement Hamiltonian of A reads [2, 49]

$$\widehat{K}_A = \sum_{i,j \in A} H_{i,j}\, c_i^\dagger c_j \tag{B.9}$$

where the $L_A \times L_A$ matrix H can be written as

$$H_{i,j} = \sum_{k=1}^{L_A} \phi_k(i)\, \varepsilon_k\, \phi_k(j) \qquad\qquad \varepsilon_k = \log\left(\frac{1-\zeta_k}{\zeta_k}\right) \tag{B.10}$$

where ε_k are the single-particle entanglement energies, while ζ_k and $\phi_k(i)$ are the eigenvalues ζ_k and the eigenvectors of C_A, which can be diagonalized numerically.

In figure 29, we show the matrix $H_{i,j}$ in (B.10) for $L_2 = 1.5L_1$ and $q_{\mathrm{F}} = \pi/2$. The green, red and black dashed curves, corresponding to (7.7), (7.9) and (7.10), respectively, are shown to facilitate the comparison with figures 14, 22 and 23 for the bosonic models explored in this article. While the green and the red dashed hyperbolae can be observed in the profile of the matrix elements of H, as already highlighted in [23], the black dashed hyperbola does not occur, in contrast with the case of a massless harmonic chain (see figure 14). This observation is further supported by figure 30, where the elements of a single row $H_{i_0,j}$ are shown, and the magnitude does not increase around the vertical dashed black segment, in contrast with the case of a massless harmonic chain (see figure 15).

The continuum limit procedure requires us to introduce the continuum spatial coordinate $x = i\, s$ in terms of the infinitesimal lattice spacing s and to perform the following replacement:

$$c_i \to \sqrt{s}\left(\mathrm{e}^{\mathrm{i} q_{\mathrm{F}} x}\psi_{\mathrm{R}}(x) + \mathrm{e}^{-\mathrm{i} q_{\mathrm{F}} x}\psi_{\mathrm{L}}(x)\right) \tag{B.11}$$

where ψ_{R} and ψ_{L} denote the right-moving and the left-moving chiral fields, respectively.

https://doi.org/10.1088/1742-5468/addaa7

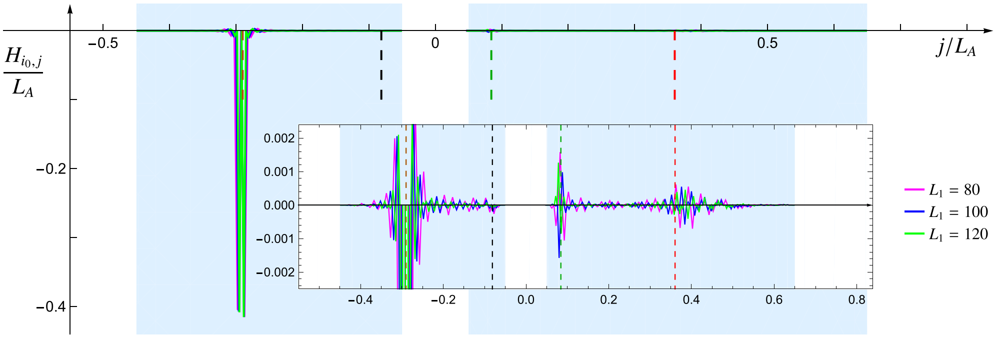

Figure 30. Matrix elements of H along a row corresponding to the site labelled by $i = i_0$. Here, $L_2 = 1.5L_1$, $i_0 = 0.4L_1$ and $\delta = 1/10$. The green, red, black and brown vertical dashed segments highlight the intersections of the row with the curves corresponding to (7.7), (7.9), (7.10) and the main diagonal, respectively (see the dashed lines in figure 29). The inset zooms in to highlight the oscillatory behaviour and the relative amplitudes around these intersections.

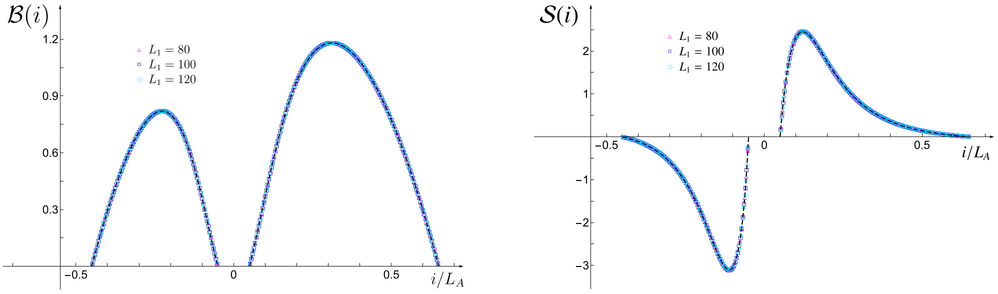

Figure 31. The combinations (B.12) (left) and (B.13) (right) for $L_2 = 1.5L_1$ and $\delta = 1/10$ for various values of L_A. The dashed curves are given by the weight functions (7.5) and (B.5), respectively.

Considering the half-filling case, where $q_{\mathrm{F}} s = \pi/2$, in [23] it has been shown that proper combinations of the matrix elements of H provide the weight functions (7.5) and (B.5) in the continuum limit. In particular, for the diagonal blocks, one considers the following combination of the matrix elements on the ith row:

$$\mathcal{B}(i) \equiv -\sum_{j\in A_k} (-1)^{(j-i)/2}\,(j-i)\,H_{i,j} \qquad i\in A_k \qquad k\in\{1,2\} \tag{B.12}$$

which is slightly different from the combination defined in equation (31) of [23], where a summation over the diagonals occurs. In the off-diagonal blocks, the combination of the matrix elements on the ith row introduced in [23] reads

$$\mathcal{S}(i) \equiv \sum_{j\in A_r} (-1)^{(j-i-1)/2}\,H_{i,j} \qquad i\in A_k \qquad r\neq k \qquad r,k\in\{1,2\}\,. \tag{B.13}$$

In figure 31, we show that (B.12) and (B.13) reproduce well the weight functions (7.5) and (B.5), respectively, in the scaling limit, as already found in [23].

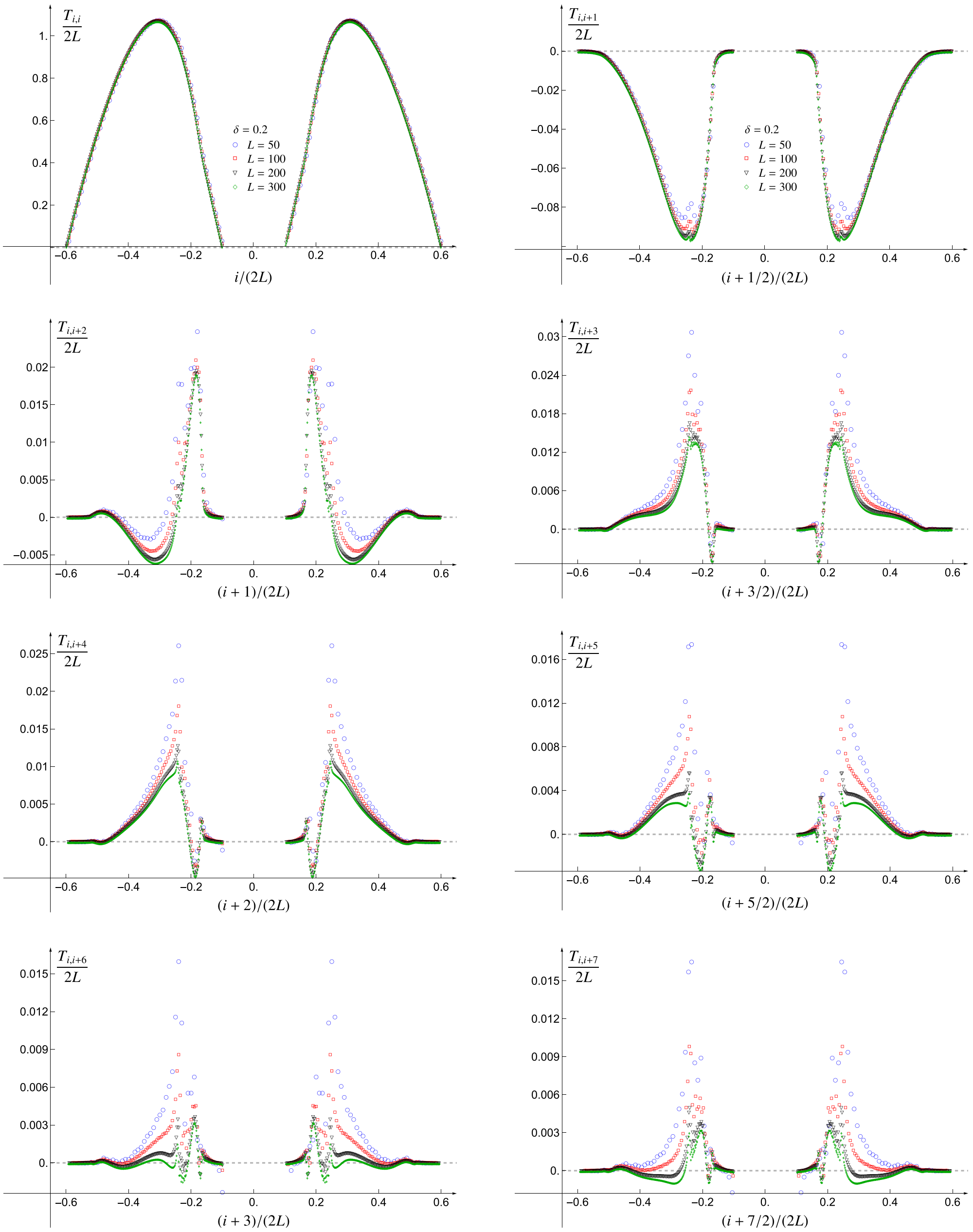

Figure 32. Diagonals of matrix T for $L_1 = L_2$ and $\omega L_A = 10^{-50}$.

Appendix C. Massless regime: further details

In this appendix, we report further numerical results supporting the observations made in section 7 for the entanglement Hamiltonian of two disjoint blocks in a massless regime.

Considering the simplest configuration of equal intervals with $L_1 = L_2 \equiv L$ in a massless regime with $\omega L_A = 10^{-50}$ and choosing $\delta = 0.2$, in figures 32 and 33 we report some numerical data showing that the functions $\tau_k(x_k)$ and $\nu_k(x_k)$, introduced in (7.15) and which involve only the elements in the diagonal blocks of T and V, are well defined.

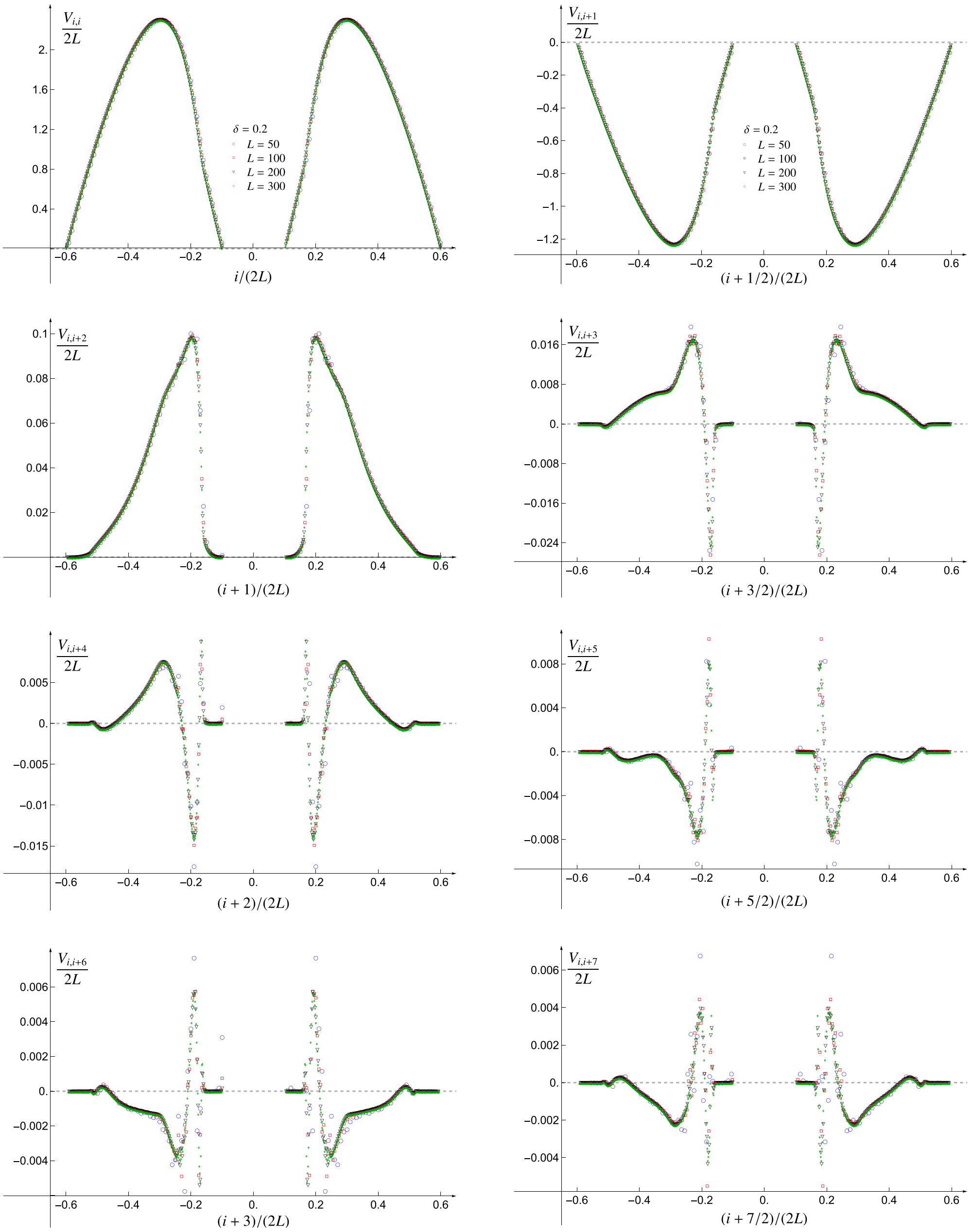

Figure 33. Diagonals of the matrix V for $L_1 = L_2$ and $\omega L_A = 10^{-50}$.

In particular, eight diagonals have been explored, *i.e.* $0 \leqslant k \leqslant 7$ in (7.15). An example with $L_2 = 2L_1$ has been considered in figure 17, only for the diagonals providing the largest contributions. The numerical results displayed in figures 32 and 33 suggest that the functions $\tau_k(x_k)$ and $\nu_k(x_k)$ are continuous but not smooth. This lack of smoothness has also been checked by exploring the discrete first derivative of $\tau_k(x_k)$ and $\nu_k(x_k)$ from the numerical data points, as was done in the right panels of figure 17, but we do not find it worth reporting these plots here.

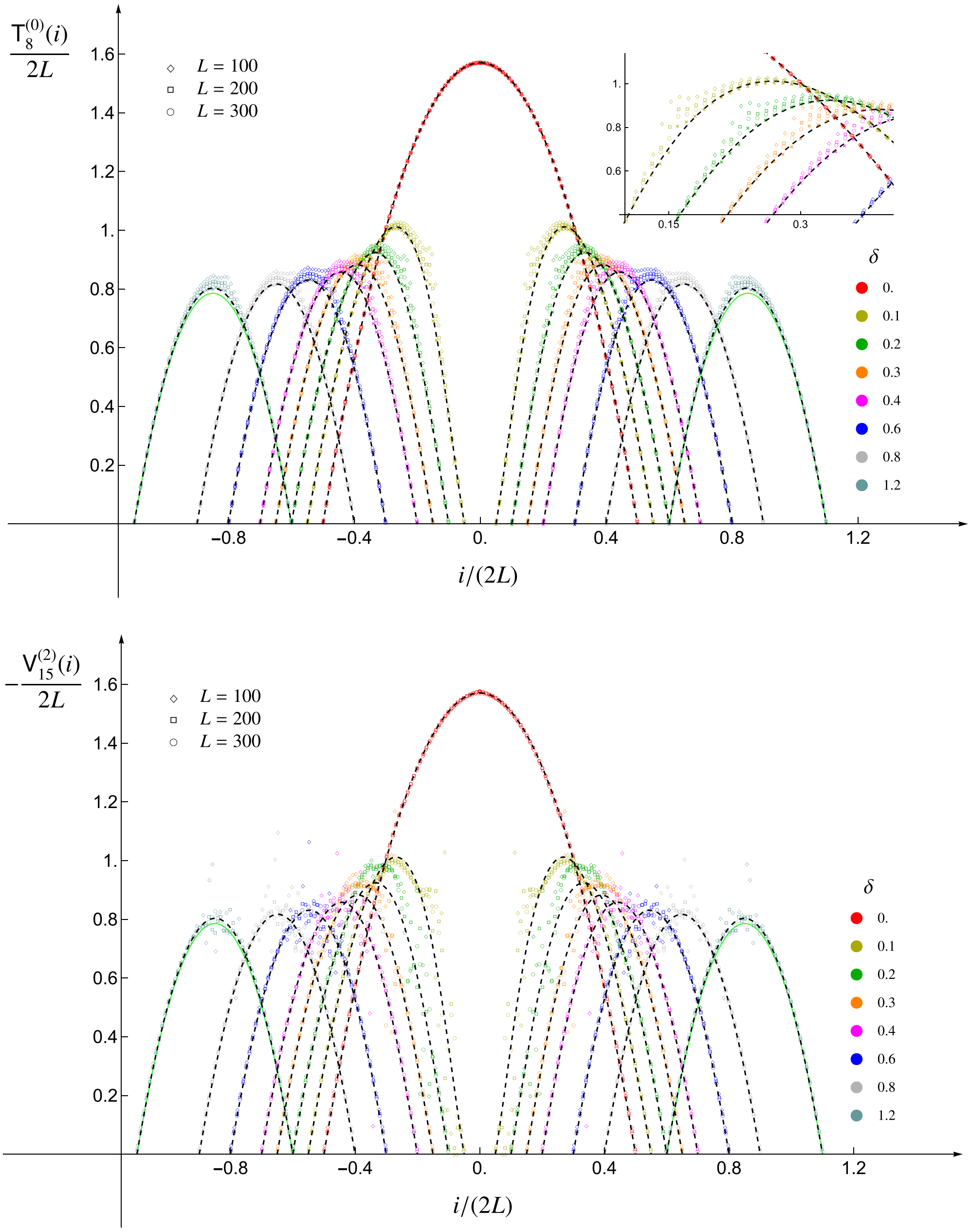

Figure 34. The combinations of diagonals defined in the first expression of (7.16) (top) and in (7.17) (bottom) for $k_{\max} \ll L_A$ (see also (7.19)) when $L_2 = L_1$ (see also figure 20). The dashed black curve corresponds to (7.5) and the solid green curve to its limit $d \to +\infty$.

Considering configurations of equal intervals and in a massless regime with $\omega L_A = 10^{-50}$, in figures 34 and 35 we report some numerical results to test the functions introduced on the left-hand side of (7.20), as was done in figures 20 and 21 for $L_2 = 2L_1$; hence, we refer the reader to the main text for a discussion of the quantities involved in this analysis. Comparing the results displayed in these four figures, one observes that

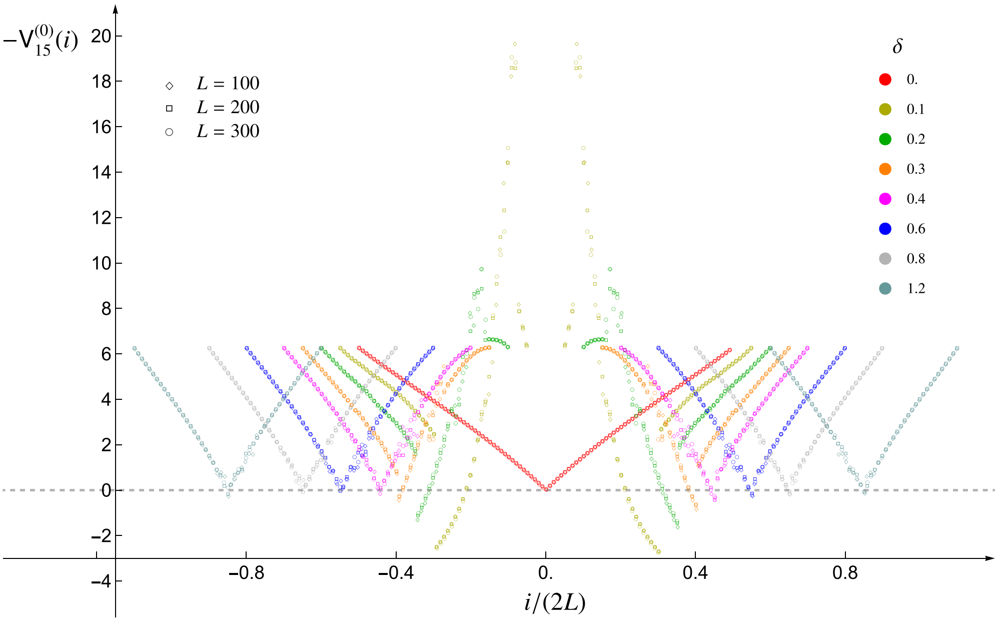

Figure 35. The combination of diagonals defined in the second expression of (7.16) for $k_{\max} \ll L_A$ (see also (7.19)) when $L_2 = L_1$ (see also figure 21).

the convergence of the data points is slightly better when subsystem A is made by equal intervals.

The consistency condition $k_{\max} \ll L_A$ is important in the limiting procedure discussed in section 7 for exploring the local term, based on the combinations of diagonals (7.16)–(7.19) (see also [15] for the single block case). For equal intervals, the role of $k_{\max}$ can be investigated by comparing the numerical data points reported in figures 34, 36 and 37. In figure 34, the values of $k_{\max}$ correspond to those where the best convergence has been observed. The most significant improvement provided by the optimal choice of $k_{\max}$ occurs in $\mathsf{V}^{(2)}_{k_{\max}}(i)/(2L)$ (see the bottom panels of these three figures). Indeed, already for adjacent intervals (*i.e.* for $\delta = 0$) when $k_{\max} = 3$ and $k_{\max} = 6$, this quantity does not provide the expected parabola.

The occurrence of a non-local term coming from the diagonal blocks of T and V might require a non-trivial modification of the limiting procedure to extract the local term.

As for the off-diagonal blocks in matrices T and V, the numerical results in figure 14 and figure 15 (see also the top and middle panels of figure 23) indicate that a large contribution comes from the elements close to the front corresponding to $x_\Gamma(x)$ in (7.9), with $x \in A$. We find it worth exploring the elements of these matrices along this front.

Since for $L_1 \neq L_2$ the function $x_\Gamma(i)$ with $i \in A$ does not provide integer numbers, a way to define this front on the lattice must be introduced. Along the ith row of either T or V, we consider the element labelled by $\lfloor x_\Gamma(i) \rfloor$ and the four elements around it, namely the five elements corresponding to $\lfloor x_\Gamma(i) \rfloor + k$ with $k \in \{-2,-1,0,1,2\}$. The minimum among these five values provides $\tilde{x}_\Gamma(i)$, which is employed in figure 39. When $L_1 = L_2$, we have $\tilde{x}_\Gamma(i) = 2L + d - i$, which corresponds to the element of the antidiagonal.

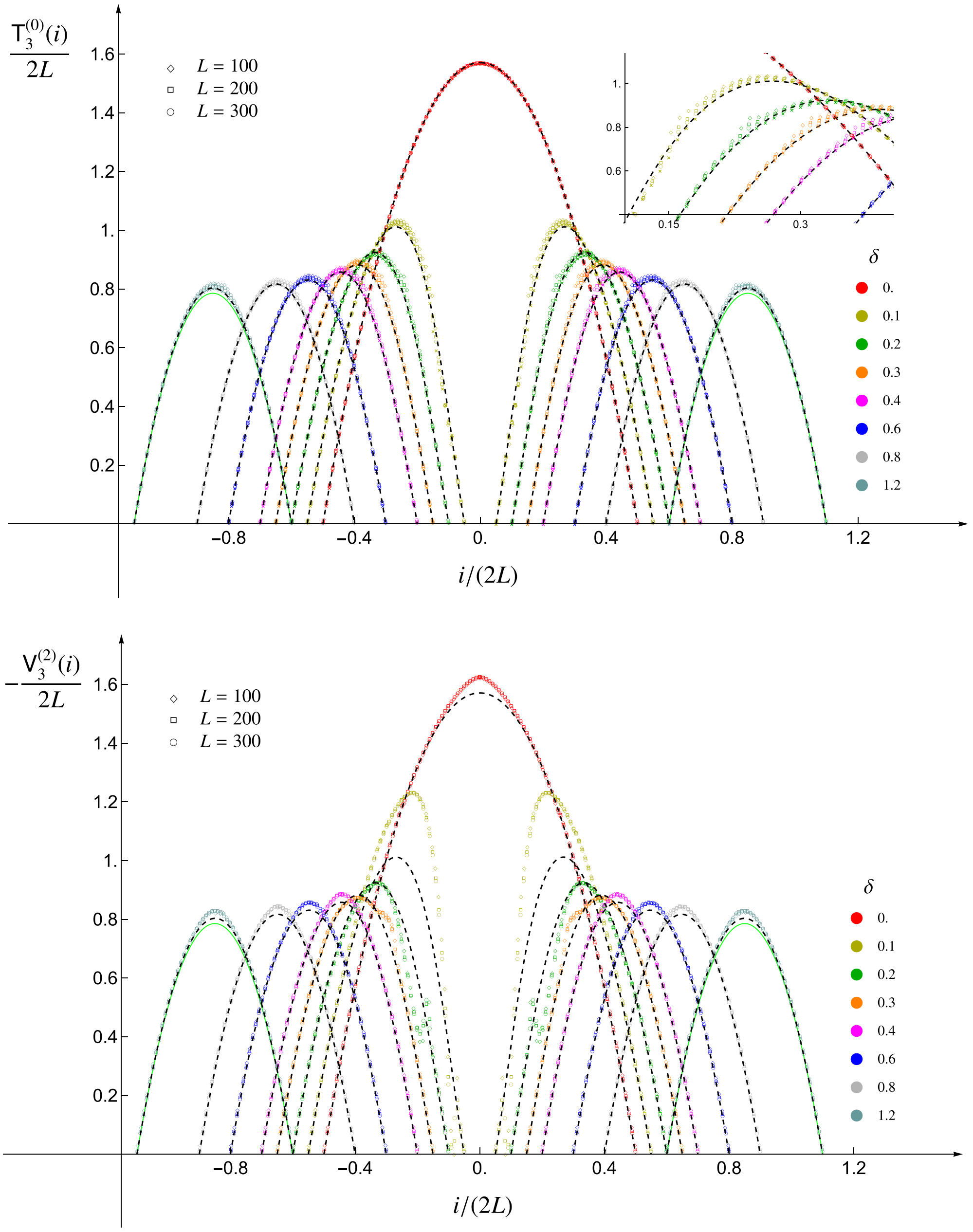

Figure 36. The combinations of diagonals displayed in figure 34 for $k_{\max} = 3$.

When $L_1 = L_2$, the expression (7.9) gives the antidiagonal of T and V and $\tilde{x}_{\mathrm{r}}(i) = 2L + d - i$. The corresponding numerical results are shown in figure 38, where the data point collapses suggest that the leading scaling behaviour with respect to the total size $2L$ of the subsystem is $T_{i,2L+d-i} \sim \log(2L)$ and $V_{i,2L+d-i} \sim \mathcal{O}(1)$. In [28], a logarithmic scaling along the antidiagonal was also observed for a chiral current (see section 8). The convergence of the numerical results for $L_1 \neq L_2$ is worse with respect to the case

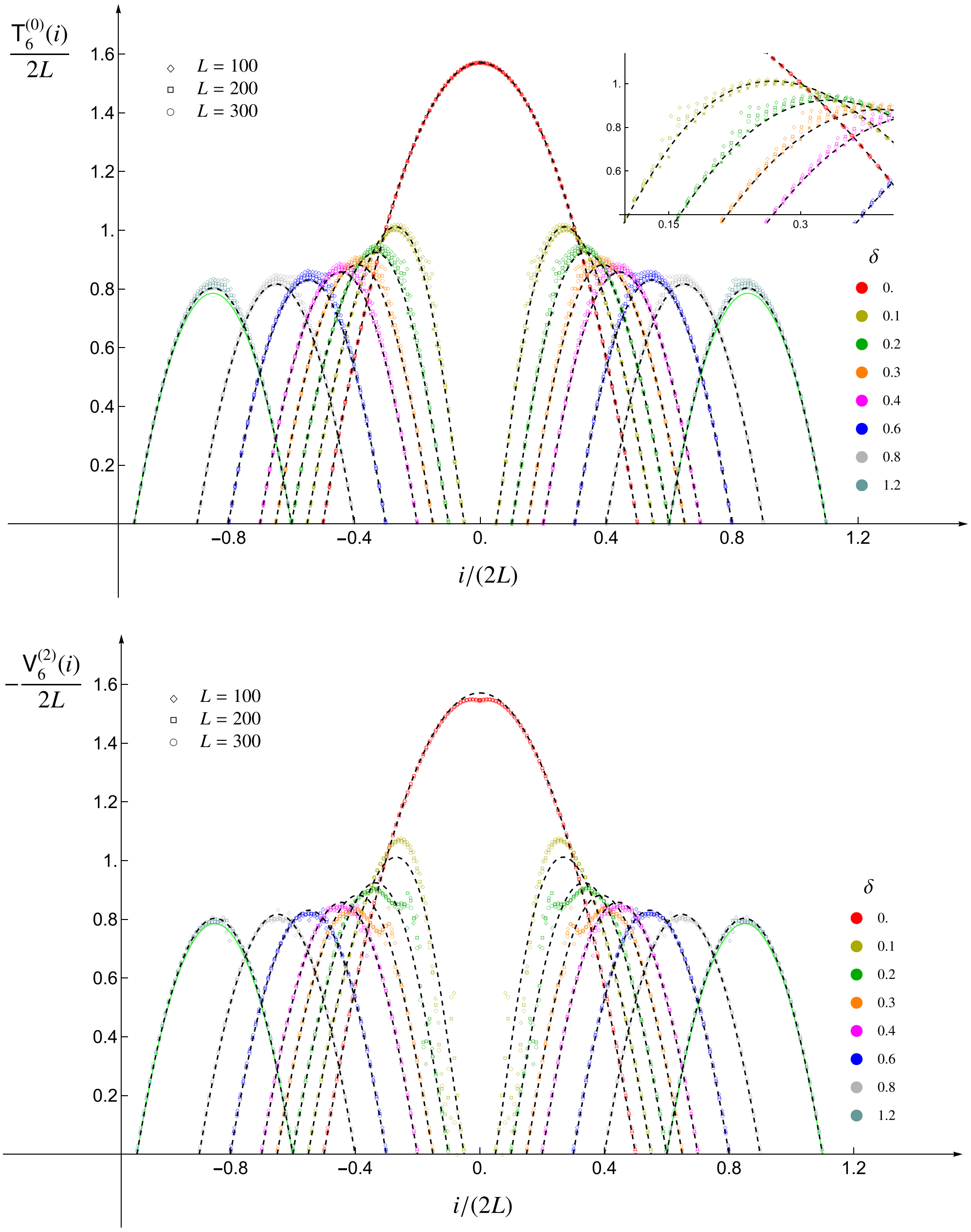

Figure 37. The combinations of diagonals displayed in figures 34 and 36 for $k_{\max} = 6$.

$L_1 = L_2$. In figure 39, we report some data for $L_2 = 2L_1$, and it seems that $T_{i,x_\Gamma(i)} \sim \log L_A$ (although the data collapses are not as good as in the case $L_1 = L_2$), while the data obtained from V do not display any clear convergence.

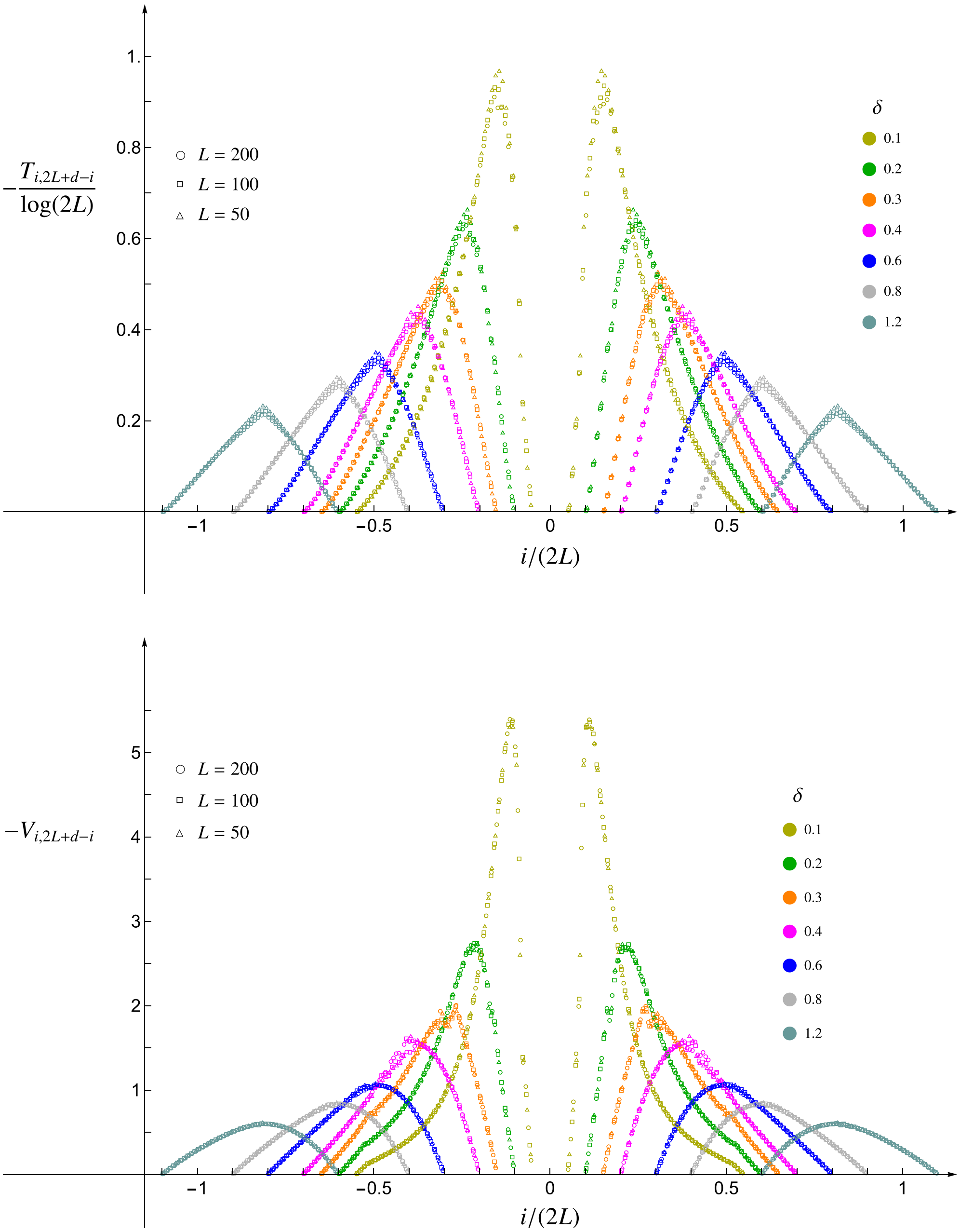

Figure 38. Antidiagonals of T (top) and V (bottom) for $L_1 = L_2$ and various separations.

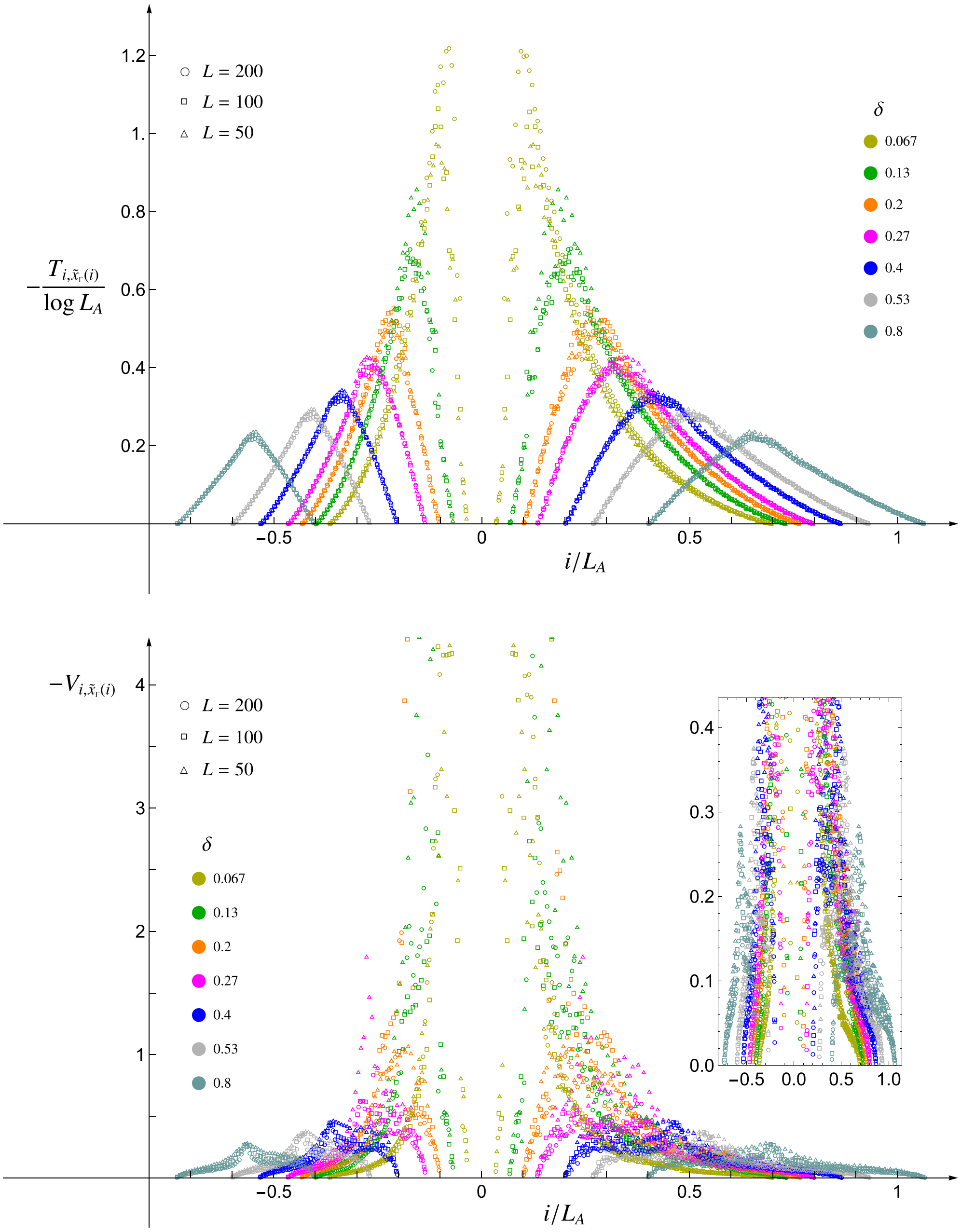

Figure 39. Elements in the off-diagonal blocks of T (top) and V (bottom) around the front identified by (7.9), as discussed in appendix C, for $L_2 = 2L_1$ and various separations.

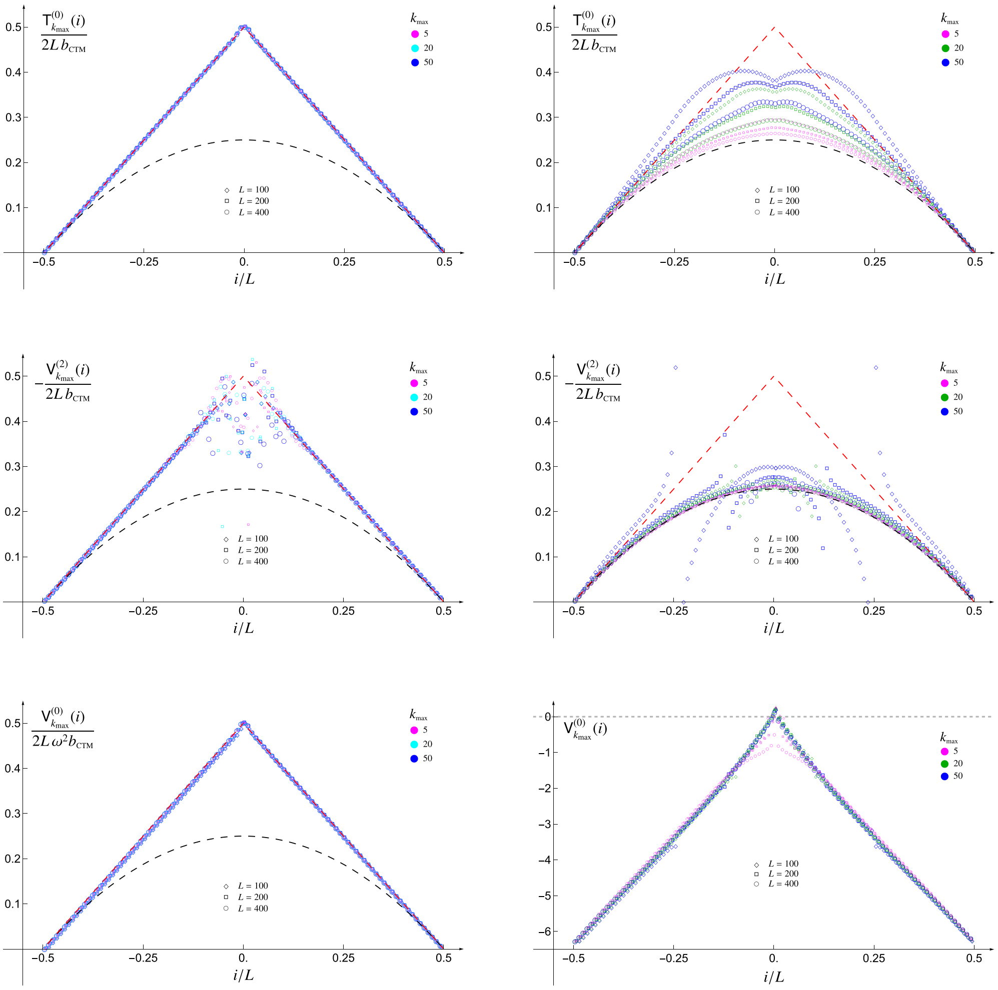

Figure 40. Combinations of diagonals given by (7.16), (7.17) and (D.1) for a fixed value of $k_{\max} \ll L$ when either $\omega L = 500$ (left) or $\omega L = 1$ (right).

Appendix D. Massive regime: single block

In order to gain some insights into massive regimes, in this appendix we investigate the entanglement Hamiltonian (2.10) of a single block A made by L contiguous sites in an infinite harmonic chain when the mass parameter takes finite and non-vanishing values. Some observations about this regime have been also made in [21].

Following [15, 16], let us consider the combinations of diagonals given by $\mathsf{T}^{(0)}_{k_{\max}}$, $\mathsf{V}^{(0)}_{k_{\max}}$ and $\mathsf{V}^{(2)}_{k_{\max}}$, introduced in (7.16) and (7.17), where, in order to take into account the simpler case of the single block that we are considering, (7.18) is replaced by

$$A_< \equiv [1\,, L/2] \qquad\qquad A_> \equiv [L/2+1\,, L]\,. \tag{D.1}$$

In our analysis, even values of L are chosen; hence, $A_<$ and $A_>$ are well defined. Notice that the definition (D.1) leads to a maximum allowed value for $k_{\max}$ given by $L/2$.

In figure 40, we report some numerical results for these combinations of diagonals when $k_{\max} \ll L$ is kept fixed while L increases. In particular, we have $\omega L = 500$ and $\omega L = 1$ in the left and right panels, respectively. The red and black dashed curves in figure 40 correspond to the triangular function [21] and to the parabolic function [8], respectively, which occur in the large mass (see section 4) and in the massless regime, respectively. In particular, the data points in the left panels are described well by the function employed in (4.6)–(4.9). The quantity considered in the bottom-left panel comes from the proper combination of both the expressions in (4.7), and only ω^2 occurs in the coefficient characterizing its slope. Moreover, we remark that the three-diagonals approximation cannot be applied for figure 40 (see also figure 10 of [21]). Taking the limit $L \to +\infty$ with $\omega L = 1$ provides a probe of the massive regime of quantum field theory in a continuum. In the top- and middle-right panels of figure 40, a collapse of the numerical data points in this regime as $L \to +\infty$ is not observed. Instead, in the bottom-right panel of the same figure, the data points of $\mathsf{V}^{(0)}_{k_{\max}}(i)$ provide a good triangular shape function, but we remark that this quantity scales in a different way with respect to the corresponding panel on the left, where the large mass regime is considered. It would be interesting to further explore this dramatic change in scaling for this quantity.

The lack of data point collapses for increasing values of L when $k_{\max}$ is kept fixed, observed in figure 40, leads us to consider a different scaling limit where the ratio $k_{\max}/L$ is kept fixed as L increases. In figure 41, we report some numerical results for the combinations of diagonals $\mathsf{T}^{(0)}_{k_{\max}}$, $\mathsf{V}^{(0)}_{k_{\max}}$ and $\mathsf{V}^{(2)}_{k_{\max}}$ in this scaling limit. In the top panels, $k_{\max}/L = 1/2$, and different values of ωL are considered. Instead, in the remaining panels, ωL is kept fixed while $k_{\max}/L$ takes different values ($\omega L = 1$ in the middle-right panel and in both the bottom panels, and $\omega L = 500$ in the middle-left panel). Besides the fact that the expected results are recovered in the limiting regimes of $\omega L \to 0^+$ and $\omega L \gg 1$, the main feature to highlight in figure 41 is given by the nice collapses of the data points for increasing values of L. These collapses suggest that this scaling limit can provide useful insights to explore the continuum limit of the entanglement Hamiltonian in a massive regime. In the middle panels, where either $\omega L = 500$ (left panel) or $\omega L = 1$ (right panel), we show that this quantity scales differently as one goes from a finite value of ωL to $\omega L \gg 1$ (see also the bottom panels of figure 40). It would also be worth further exploring this change in the scaling in the setting where the ratio $k_{\max}/L$ is kept fixed while $L \to +\infty$. In the bottom panels of figure 41, the combinations of diagonals $\mathsf{T}^{(0)}_{k_{\max}}$ and $\mathsf{V}^{(2)}_{k_{\max}}$ are considered; we obtain well-defined curves for different values of $k_{\max}/L$ for both these quantities, but those corresponding to $\mathsf{V}^{(2)}_{k_{\max}}$ display two singularities.

The data collapses, the singular behaviour of the curves and the fact that the triangular function is not an upper bound for them, observed in figure 41, suggest we should consider the same scaling limit for different combinations of diagonals. A possibility is to modify (7.16) and (7.17) by introducing, respectively,

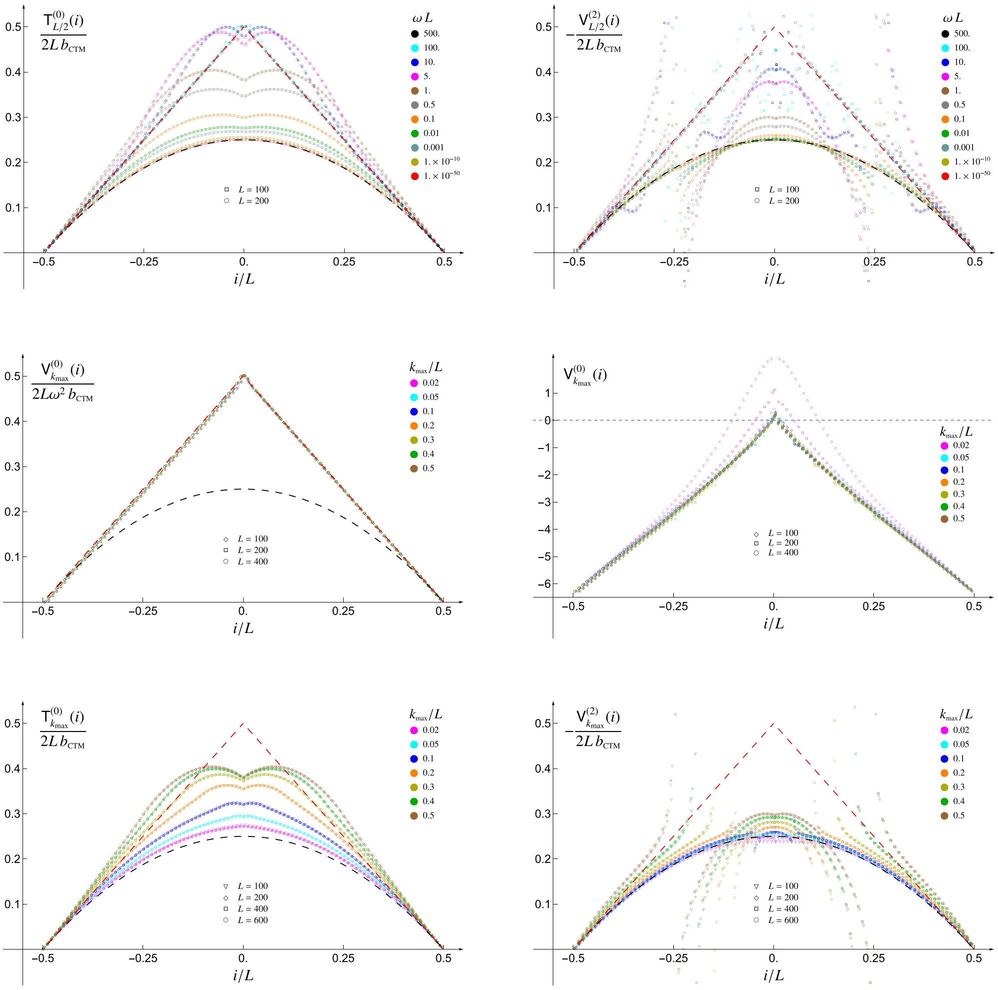

Figure 41. Combinations of diagonals in (7.16), (7.17) and (D.1) for fixed $k_{\max}/L$ and ωL.

$$\widetilde{\mathsf{T}}^{(0)}_{k_{\max}}(i) \equiv \begin{cases} T_{i,i} + 2\displaystyle\sum_{k=1}^{k_{\max}} T_{i,i-k} \\ T_{i,i} + 2\displaystyle\sum_{k=1}^{k_{\max}} T_{i+k,i} \end{cases} \qquad \widetilde{\mathsf{V}}^{(0)}_{k_{\max}}(i) \equiv \begin{cases} V_{i,i} + 2\displaystyle\sum_{k=1}^{k_{\max}} V_{i,i-k} & i \in A_< \\ V_{i,i} + 2\displaystyle\sum_{k=1}^{k_{\max}} V_{i+k,i} & i \in A_> \end{cases} \tag{D.2}$$

and

$$\widetilde{\mathsf{V}}^{(2)}_{k_{\max}}(i) \equiv \begin{cases} \displaystyle\sum_{k=1}^{k_{\max}} k^2\, V_{i,i-k} & i \in A_< \\ \displaystyle\sum_{k=1}^{k_{\max}} k^2\, V_{i+k,i} & i \in A_> \end{cases} \tag{D.3}$$

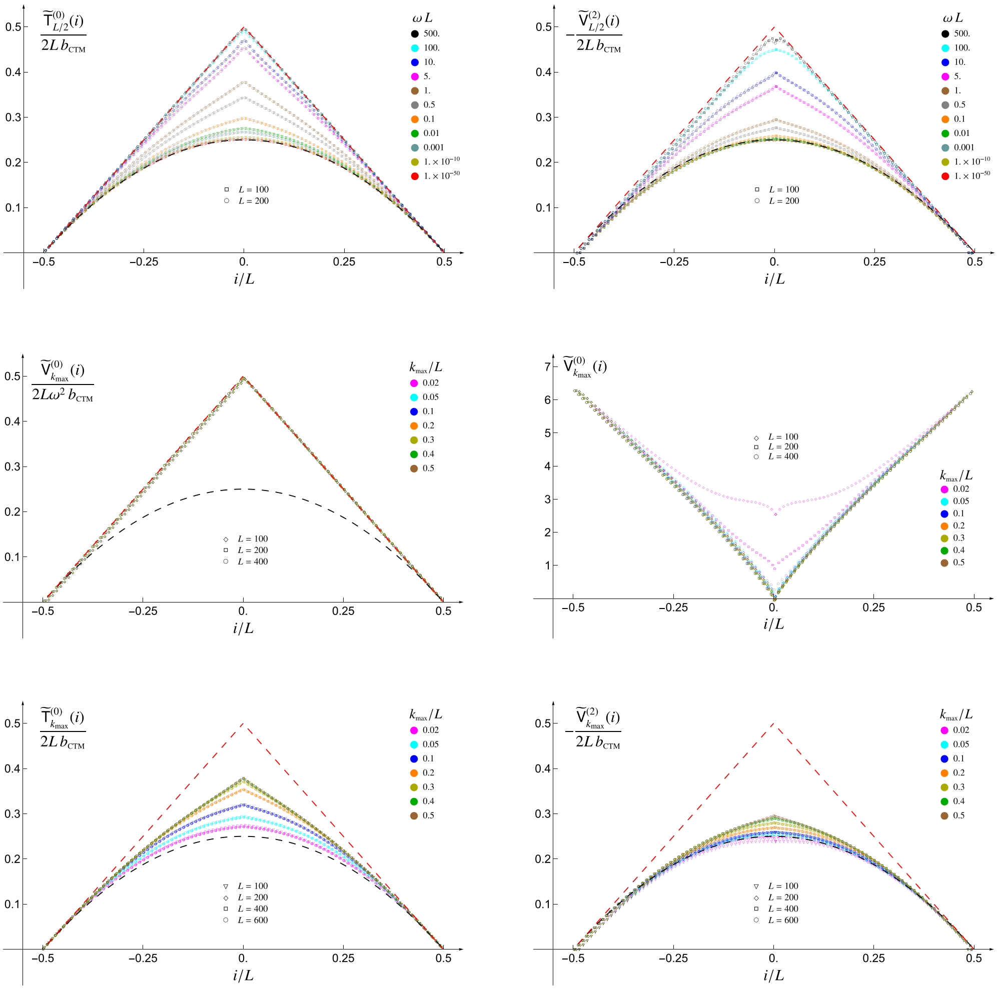

Figure 42. Combinations (D.2), (D.3) and (D.1) for when $k_{\max}/L$ and ωL are kept fixed (see also figure 41).

where (D.1) is employed to define the range of the index i, imposing that the sums stop when $i-k \leqslant 0$ or $i+k > L$.

In figure 42, we report numerical results for the combinations of diagonals $\widetilde{\mathsf{T}}^{(0)}_{k_{\max}}$, $\widetilde{\mathsf{V}}^{(0)}_{k_{\max}}$ and $\widetilde{\mathsf{V}}^{(2)}_{k_{\max}}$, introduced in (D.2) and (D.3), in the same setup, choices of the parameters and scheme for the panels considered in figure 41. For these combinations, data collapses are also observed, and the expected curves are recovered in the limiting regimes of $\omega L \to 0^+$ and $\omega L \gg 1$. Comparing figures 42 and 41, we remark that the triangular and parabolic functions, characterizing the $\omega L \to 0^+$ and $\omega L \gg 1$ regimes, respectively, provide a lower bound and an upper bound for the curves obtained from (D.2) and (D.3) when ωL takes finite and non-vanishing values. When $\omega L = 1$, the curve in the middle-right panel of figure 42 corresponds to the one obtained in the middle-right panel of figure 41 or in the bottom-right panel of figure 40 with the sign flipped.

Appendix E. Details on the free chiral current model

In this appendix, we discuss some features of the free chiral current model [30], and, following [28], we review some technical details about the numerical evaluation of the entanglement Hamiltonian matrix H, whose results are discussed in section 8.

Consider the lattice Hamiltonian $H=\frac{1}{2}\sum_{i=1}^{L} b_i$ on a circle [30]. At a classical level, the variables b_i satisfy the unusual Poisson brackets given by $\big\{b_i, b_j\big\} = \delta_{i,j+1} - \delta_{i,j-1}$, and the equation of motion reads $\dot{b}_i = \big\{b_i, H\big\} = b_{i-1} - b_{i+1}$. This equation admits plane wave solutions $b_i = \exp[\mathrm{i}(ki - Et)]$ with the dispersion relation $E(k) = 2\sin(k)$, whose periodicity allows us to restrict the domain of the quasi-momentum to $k \in [0, 2\pi]$. Since $E(0) = E(\pi) = 0$, two values of k correspond to the same extremal value of $E(k)$. Moreover, the group velocities $\partial_k E|_{k=0} = -\partial_k E|_{k=\pi} = 2$ around these values have the opposite sign; hence, the model contains both left-moving and right-moving excitations, corresponding to the modes around $k=0$ and $k=\pi$, respectively. This feature can be clarified by defining the variables $\tilde{b}_i = (-1)^i\, b_i$, which satisfy $\big\{\tilde{b}_i, \tilde{b}_j\big\} = -\big\{b_i, b_j\big\} = \delta_{i,j-1} - \delta_{i,j+1}$ and give $\tilde{b}_i = \exp[\mathrm{i}((k+\pi)i - Et)]$ for the plane wave solution. Each left-moving excitation having $k \in [0, \pi/2] \cup [3\pi/2, 2\pi]$ encoded in b_i can be associated with a right-moving solution encoded in $\tilde{b}_i$. The above-mentioned Hamiltonian can be written in terms of both types of excitations as $H = \frac{1}{4}\sum_{i=1}^{L}\big(b_i^2 + \tilde{b}_i^2\big)$.

The quantization procedure, which transforms the classical variables into operators $b_i \to \hat{b}_i$ and the Poisson brackets into commutators, preserves these features of the excitation spectrum. Considering also the operators $\hat{\tilde{b}}_i$ coming from $\tilde{b}_i$, we have $[\hat{b}_i, \hat{\tilde{b}}_j] = 0$. In the continuum limit, the relevant values of k are the minima of $|E(k)|$, namely $k=0$ and $k=\pi$. The resulting model is the sum of two chiral quantum field theories corresponding to the left- and right-moving excitations mentioned above.

In order to explore the entanglement Hamiltonian in the free chiral current model, following [28], we consider the $L_A \times L_A$ matrices Y_A and B_A introduced in section 8, with even L_A. As for Y_A, since L_A is even, the $L_A \times L_A$ orthogonal matrix O and matrix E with the same size can be constructed such that

$$E\,O\,Y_A\,O^{\mathrm{t}}E = \begin{pmatrix} \mathbf{0} & \mathbf{1} \\ -\mathbf{1} & \mathbf{0} \end{pmatrix} \equiv J \qquad\qquad E = \begin{pmatrix} X & \mathbf{0} \\ \mathbf{0} & X \end{pmatrix} \tag{E.1}$$

where X is a diagonal matrix with strictly positive real numbers on its main diagonal. The matrices O and E allow us to introduce the following canonical operators:

$$\hat{r}_i = \widetilde{O}_{i,j}\,\hat{b}_j \qquad\qquad \widetilde{O} \equiv E\,O \qquad\qquad [\hat{r}_i, \hat{r}_j] = \mathrm{i}J_{i,j} \tag{E.2}$$

where $\widetilde{O}$ is neither an orthogonal nor a symplectic matrix. The corresponding correlators $\langle \hat{r}_i\, \hat{r}_j\rangle$ provide the $L_A \times L_A$ real and symmetric matrix $\tilde{\gamma}_A$ as follows (notice that $E^{\mathrm{t}} = -E$):

$$\langle \hat{r}_i\, \hat{r}_j\rangle = \widetilde{O}\,B_A\,\widetilde{O}^{\mathrm{t}} \qquad\qquad (\tilde{\gamma}_A)_{i,j} \equiv \mathrm{Re}\,[\langle \hat{r}_i\, \hat{r}_j\rangle] \qquad\qquad \tilde{\gamma}_A = \widetilde{O}\,[\mathrm{Re}\,B_A]\,\widetilde{O}^{\mathrm{t}} \equiv \begin{pmatrix} \widetilde{Q} & S \\ S^{\mathrm{t}} & \widetilde{P} \end{pmatrix}. \tag{E.3}$$

https://doi.org/10.1088/1742-5468/addaa7

The matrix $\tilde{\gamma}_A$ is positive definite for all the cases that we have considered, although this feature has been checked only numerically. Assuming that $\tilde{\gamma}_A$ is positive definite, its Williamson decomposition reads

$$\tilde{\gamma}_A = W^{\mathrm{t}}\left(\widetilde{D}\oplus\widetilde{D}\right)W \tag{E.4}$$

where W is a $L_A \times L_A$ real symplectic matrix, and $\widetilde{D}$ is the $(L_A/2)\times(L_A/2)$ diagonal matrix containing the symplectic spectrum $\{\tilde{\sigma}_1,\dots,\tilde{\sigma}_{L_A/2}\}$ of $\tilde{\gamma}_A$ on its diagonal, satisfying $\tilde{\sigma}_k > 0$, which can be obtained from the spectrum of $(\mathrm{i}J\tilde{\gamma}_A)^2$ in a standard way [48]. This symplectic spectrum provides the Rényi entropies and the entanglement entropy through (2.8) and (2.9), respectively.

The matrix R_A introduced in (8.4) is related to $\tilde{\gamma}_A$. Indeed, by inverting (E.1), one first observes that $Y_A^{-1} = -\widetilde{O}^{\mathrm{t}} J^{\mathrm{t}}\,\widetilde{O}$. Then, combining this expression with (8.4), we get

$$R_A\, Y_A^{-1} = \mathrm{i}\,\widetilde{O}^{\mathrm{t}}\, J^{\mathrm{t}}\,\tilde{\gamma}_A J\,\widetilde{O} \tag{E.5}$$

and

$$R_A^2 = -Y_A^{-1}\,(\mathrm{Re}B_A)\,Y_A^{-1}\,(\mathrm{Re}B_A) = \widetilde{O}^{\mathrm{t}}\,(\mathrm{i}J\tilde{\gamma}_A)^2\,\widetilde{O}^{-\mathrm{t}}\,. \tag{E.6}$$

The entanglement Hamiltonian can then be written in terms of either $\hat{r}_i$ or $\hat{b}_i$ as follows:

$$\widehat{K}_A = \frac{1}{2}\,\hat{\boldsymbol{r}}^{\mathrm{t}}\,N_A\,\hat{\boldsymbol{r}} = \hat{\boldsymbol{b}}^{\mathrm{t}} M\,\hat{\boldsymbol{b}} \tag{E.7}$$

where N_A reads [3] (see also [56])

$$N_A = h\left(\sqrt{(\mathrm{i}J\tilde{\gamma}_A)^2}\right)\,J^{\mathrm{t}}\,\tilde{\gamma}_A\,J \tag{E.8}$$

in terms of $h(y)$ defined in (2.13), while matrix M has been introduced in (8.5), and it can be obtained by using (E.5) and (E.6) in (E.8).

The entanglement Hamiltonian (E.7) can be written as follows:

$$\widehat{K}_A = \begin{pmatrix} \hat{\boldsymbol{b}}^{\mathrm{t}} \\ \hat{\tilde{\boldsymbol{b}}}^{\mathrm{t}} \end{pmatrix} \begin{pmatrix} M/2 & 0 \\ 0 & \widetilde{M}/2 \end{pmatrix} \begin{pmatrix} \hat{\boldsymbol{b}} \\ \hat{\tilde{\boldsymbol{b}}} \end{pmatrix} \tag{E.9}$$

where $\widetilde{M}_{i,j} = (-1)^{i+j} M_{i,j}$ and $\hat{\tilde{b}}_i = (-1)^i\,\hat{b}_i$. Notice that $M_{i,i+2k+1} = 0$ because of the parity symmetry [30]; hence, $\widetilde{M} = M$.

In the continuum limit, which requires the UV cutoff a, we have $\hat{b}_i \to a j(x)$ and $\hat{\tilde{b}}_i \to a\bar{j}(x)$ for the operators and $M_{ij}/2 \to H(x,y)$ for the matrix, where $i\,a \to x$ and $j\,a \to y$. The chiral fields coming from the left- and right-moving excitations are also decoupled in the entanglement Hamiltonian, which is therefore given by the sum of the corresponding operators associated with these two different types of excitations.

Appendix F. Rényi mutual information

The Rényi mutual information for the bipartition of the line given by $A = A_1 \cup A_2$ is a UV finite quantity defined as the following combination of Rényi entropies:

$$I^{(n)}_{A_1,A_2} = S^{(n)}_{A_1} + S^{(n)}_{A_1} - S^{(n)}_{A_1 \cup A_2} \tag{F.1}$$

where $n \geqslant 0$ is an integer, and its analytic continuation $n \to 1$ gives the mutual information I_{A_1,A_2}. In this appendix, we discuss the Rényi mutual information (F.1) for a (uncompactified) massless scalar field [35] and a chiral current [28], whose underlying lattice models have been described in sections 2 and 8, respectively. In these CFT models, the Rényi mutual information (F.1) is a function of the harmonic ratio of the four endpoints of A, namely

$$\eta \equiv \frac{(v_1 - u_1)\,(v_2 - u_2)}{(u_2 - u_1)\,(v_2 - v_1)} \tag{F.2}$$

where $A_j = (u_j, v_j)$ for $j \in \{1,2\}$ [34, 35].

The Rényi mutual information (F.1) for the massless scalar reads [35]

$$I^{(n)}_{A_1,A_2;(\mathrm{ms})} = -\frac{n+1}{6n} \log(1-\eta) + \frac{D_n(\eta) + D_n(1-\eta)}{2(1-n)} \tag{F.3}$$

where

$$D_n(\eta) \equiv \sum_{k=1}^{n-1} \log[{}_2F_1(k/n, 1-k/n; 1; \eta)] \,. \tag{F.4}$$

Taking the analytic continuation $n \to 1$ of (F.3), one obtains the mutual information

$$I_{A_1,A_2;(\mathrm{ms})} = -\frac{1}{3} \log(1-\eta) + \frac{D_1'(\eta) + D_1'(1-\eta)}{2} \tag{F.5}$$

where

$$D_1'(\eta) \equiv \lim_{n \to 1} \frac{D_n(\eta)}{1-n} = -\int_{-\mathrm{i}\infty}^{\mathrm{i}\infty} \frac{\pi z}{\mathrm{i}\,[\sin(\pi z)]^2} \log[{}_2F_1(z, 1-z; 1; \eta)]\, \mathrm{d}z \,. \tag{F.6}$$

Discarding the logarithmic term in the RHSshs of (F.3) and (F.5), the resulting expression is invariant under exchange $\eta \leftrightarrow 1-\eta$, indicating that this model satisfies the Haag duality [35].

In figure 43, we show some numerical data for the Rényi mutual information (F.1) of equal blocks of size L for a massless harmonic chain, evaluated by using (2.8), with $\omega L_A = 10^{-50}$. The agreement between the data points and the solid curves obtained from (F.3) and (F.5), for $n \neq 1$ and $n = 1$, respectively, provides an important check for the analysis of [35].

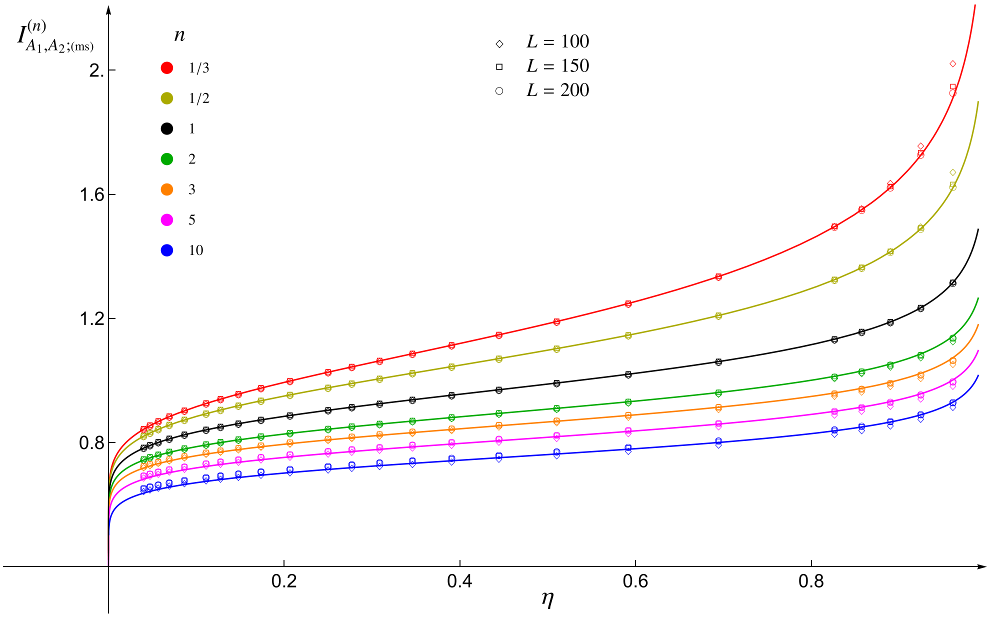

Figure 43. Rényi mutual information of equal blocks of length L for a massless scalar. Here, $\omega L_A = 10^{-50}$.

The Rényi mutual information (F.1) in the chiral current model (see section 8) reads [28]

$$I^{(n)}_{A_1,A_2;(\mathrm{cc})} = -\frac{n+1}{12\,n}\log(1-\eta) + U_n(\eta) \tag{F.7}$$

where

$$U_n(\eta) \equiv \frac{\mathrm{i}\,n}{2(n-1)}\int_0^{+\infty}\left[\coth(\pi\, sn) - \coth(\pi\, s)\right]\log\left(\frac{{}_2F_1(1+i\,s,-i\,s;1;\eta)}{{}_2F_1(1-i\,s,i\,s;1;\eta)}\right)\mathrm{d}s\,. \tag{F.8}$$

The analytic continuation $n\to 1$ of (F.7) provides the mutual information for this model

$$I_{A_1,A_2;(\mathrm{cc})} = -\frac{1}{6}\log(1-\eta) + U(\eta) \tag{F.9}$$

where

$$U(\eta) \equiv \lim_{n\to 1} U_n(\eta) = -\frac{\mathrm{i}\,\pi}{2}\int_0^{+\infty}\frac{s}{\left[\sinh(\pi\, s)\right]^2}\,\log\left(\frac{{}_2F_1(1+i\,s,-i\,s;1;\eta)}{{}_2F_1(1-i\,s,i\,s;1;\eta)}\right)\mathrm{d}s\,. \tag{F.10}$$

In figure 44, we consider the Rényi mutual information for various values of n, including the $n\to 1$ case corresponding to the mutual information, by comparing the numerical data points obtained from the lattice model (by using (F.1), (2.8) and (2.9), as discussed in appendix E) against the analytic result in the continuum [28] given by (F.7) and (F.9). The lattice results have been divided by a factor of 2, in order to take into account the fact that the continuum limit of the lattice model (8.1) is described

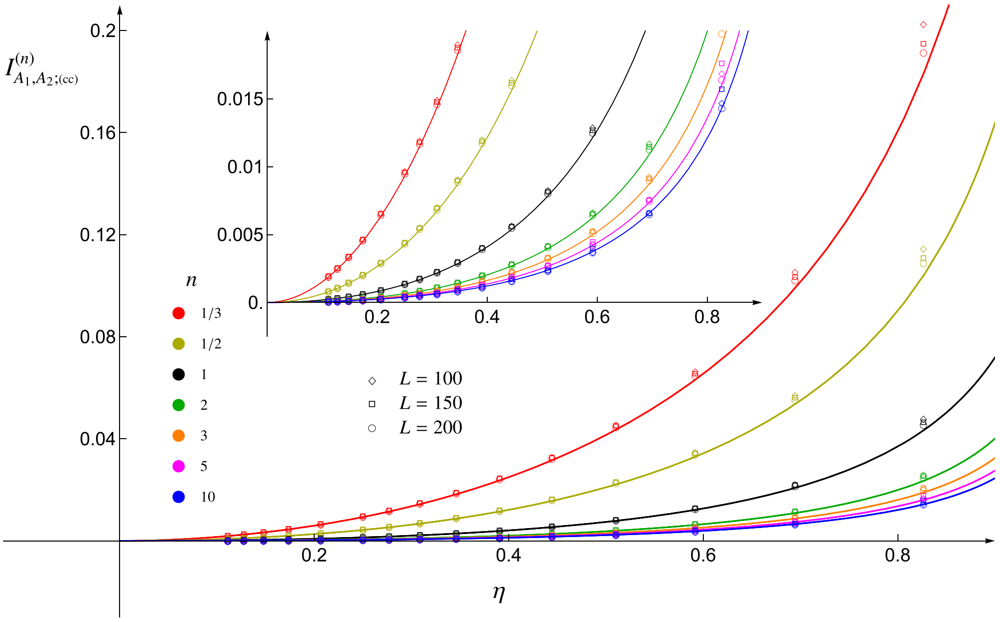

Figure 44. Rényi mutual information of equal blocks of length L for a chiral current.

by two chiral currents (see appendix E). A good agreement between the lattice data points as L increases and the corresponding analytic expressions in the continuum is observed.

It is straightforward to realize that (F.4) and (F.8) are related as follows:

$$U_n(\eta) = \frac{D_n(\eta)}{2(1-n)} \tag{F.11}$$

which can be checked numerically. The special case of (F.11) corresponding to $n \to 1$, namely $U(\eta) = D_1'(\eta)/2$, can easily be shown by performing the change of variable $s = \mathrm{i}z$. This relation, combined with (F.5) and (F.9), leads to the following relation between the mutual information of these two models:

$$I_{A_1,A_2;(\mathrm{ms})} - I_{A_1,A_2;(\mathrm{cc})} = -\frac{1}{6}\log(1-\eta) + U(1-\eta)\,. \tag{F.12}$$

Considering the RHSshs of (F.7) and (F.9), since the functions $U_n(1-\eta)$ and $U(1-\eta)$ are not invariant under the exchange $\eta \leftrightarrow 1-\eta$, the chiral current model does not satisfy Haag duality, as discussed in [28].

References

[1] Haag R 1996 *Local Quantum Physics: Fields, Particles, Algebras* (Springer)
[2] Eisler V and Peschel I 2009 Reduced density matrices and entanglement entropy in free lattice models *J. Phys. A* **42** 504003
[3] Casini H and Huerta M 2009 Entanglement entropy in free quantum field theory *J. Phys. A* **42** 504007

[4] Bisognano J and Wichmann E 1975 On the duality condition for a hermitian scalar field *J. Math. Phys.* **16** 985

[5] Bisognano J and Wichmann E 1976 On the duality condition for quantum fields *J. Math. Phys.* **17** 303

[6] Peschel I and Truong T 1991 Corner transfer matrices for the Gaussian model *Ann. Phys., Lpz.* **503** 185

[7] Peschel I and Chung M 1999 Density matrices for a chain of oscillators *J. Phys. A* **32** 8419

[8] Hislop P and Longo R 1982 Modular structure of the local algebras associated with the free massless scalar field theory *Commun. Math. Phys.* **84** 71

[9] Casini H, Huerta M and Myers R 2011 Towards a derivation of holographic entanglement entropy *J. High Energy Phys.* JHEP05(2011)036

[10] Wong G, Klich I, Pando Zayas L and Vaman D 2013 Entanglement temperature and entanglement entropy of excited states *J. High Energy Phys.* JHEP12(2013)020

[11] Cardy J and Tonni E 2016 Entanglement hamiltonians in two-dimensional conformal field theory *J. Stat. Mech.* 123103

[12] Arias R, Blanco D, Casini H and Huerta M 2017 Local temperatures and local terms in modular Hamiltonians *Phys. Rev. D* **95** 065005

[13] Eisler V and Peschel I 2017 Analytical results for the entanglement Hamiltonian of a free-fermion chain *J. Phys. A* **50** 284003

[14] Eisler V and Peschel I 2018 Properties of the entanglement Hamiltonian for finite free-fermion chains *J. Stat. Mech.* 104001

[15] Di Giulio G and Tonni E 2020 On entanglement hamiltonians of an interval in massless harmonic chains *J. Stat. Mech.* 033102

[16] Javerzat N and Tonni E 2022 On the continuum limit of the entanglement Hamiltonian of a sphere for the free massless scalar field *J. High Energy Phys.* JHEP02(2022)086

[17] Eisler V, Tonni E and Peschel I 2019 On the continuum limit of the entanglement Hamiltonian *J. Stat. Mech.* 073101

[18] Longo R and Morsella G 2023 The massless modular Hamiltonian *Commun. Math. Phys.* **400** 1181

[19] Bostelmann H, Cadamuro D and Minz C 2023 On the mass dependence of the modular operator for a double cone *Ann. Henri Poincare* **24** 3031

[20] Cadamuro D, Fröb M and Minz C 2023 Modular Hamiltonian for fermions of small mass (arXiv:2312.04629)

[21] Eisler V, Di Giulio G, Tonni E and Peschel I 2020 Entanglement Hamiltonians for non-critical quantum chains *J. Stat. Mech.* 103102

[22] Casini H and Huerta M 2009 Reduced density matrix and internal dynamics for multicomponent regions *Class. Quantum Grav.* **26** 185005

[23] Eisler V, Tonni E and Peschel I 2022 Local and non-local properties of the entanglement Hamiltonian for two disjoint intervals *J. Stat. Mech.* 083101

[24] Mintchev M and Tonni E 2021 Modular Hamiltonians for the massless Dirac field in the presence of a boundary *J. High Energy Phys.* JHEP03(2021)204

[25] Mintchev M and Tonni E 2021 Modular Hamiltonians for the massless Dirac field in the presence of a defect *J. High Energy Phys.* JHEP03(2021)205

[26] Blanco D and Pérez-Nadal G 2019 Modular Hamiltonian of a chiral fermion on the torus *Phys. Rev. D* **100** 025003

[27] Fries P and Reyes I 2019 Entanglement spectrum of chiral fermions on the torus *Phys. Rev. Lett.* **123** 211603

[28] Arias R, Casini H, Huerta M and Pontello D 2018 Entropy and modular Hamiltonian for a free chiral scalar in two intervals *Phys. Rev. D* **98** 125008

[29] Sonnenschein J 1988 Chiral bosons *Nucl. Phys. B* **309** 752

[30] Berenstein D 2023 Staggered bosons *Phys. Rev. D* **108** 074509

[31] Dalmonte M, Eisler V, Falconi M and Vermersch B 2022 Entanglement Hamiltonians: from field theory to lattice models and experiments *Ann. Phys.* **534** 2200064

[32] Calabrese P and Cardy J 2004 Entanglement entropy and quantum field theory *J. Stat. Mech.* 06002

[33] Caraglio M and Gliozzi F 2008 Entanglement entropy and twist fields *J. High Energy Phys.* JHEP11(2008)076

[34] Furukawa S, Pasquier V and Shiraishi J 2009 Mutual information and compactification radius in a c = 1 critical phase in one dimension *Phys. Rev. Lett.* **102** 170602

[35] Calabrese P, Cardy J and Tonni E 2009 Entanglement entropy of two disjoint intervals in conformal field theory *J. Stat. Mech.* 11001

[36] Calabrese P, Cardy J and Tonni E 2011 Entanglement entropy of two disjoint intervals in conformal field theory II *J. Stat. Mech.* 01021

[37] Coser A, Tagliacozzo L and Tonni E 2014 On Rényi entropies of disjoint intervals in conformal field theory *J. Stat. Mech.* 01008

[38] De Nobili C, Coser A and Tonni E 2015 Entanglement entropy and negativity of disjoint intervals in CFT: some numerical extrapolations *J. Stat. Mech.* 06021

[39] Grava T, Kels A and Tonni E 2021 Entanglement of two disjoint intervals in conformal field theory and the 2D Coulomb gas on a lattice *Phys. Rev. Lett.* **127** 141605

[40] Ryu S and Takayanagi T 2006 Holographic derivation of entanglement entropy from AdS/CFT *Phys. Rev. Lett.* **96** 181602

[41] Ryu S and Takayanagi T 2006 Aspects of holographic entanglement entropy *J. High Energy Phys.* JHEP08(2006)045

[42] Hubeny V and Rangamani M 2008 Holographic entanglement entropy for disconnected regions *J. High Energy Phys.* JHEP03(2008)006

[43] Headrick M 2010 Entanglement Renyi entropies in holographic theories *Phys. Rev. D* **82** 126010

[44] Tonni E 2011 Holographic entanglement entropy: near horizon geometry and disconnected regions *J. High Energy Phys.* JHEP05(2011)004

[45] Fonda P, Giomi L, Salvio A and Tonni E 2015 On shape dependence of holographic mutual information in AdS$_4$ *J. High Energy Phys.* JHEP02(2015)005

[46] Botero A and Reznik B 2004 Spatial structures and localization of vacuum entanglement in the linear harmonic chain *Phys. Rev. A* **70** 052329

[47] Eisert J, Cramer M and Plenio M 2010 Area laws for the entanglement entropy – a review *Mod. Phys.* **82** 277

[48] Weedbrook C, Pirandola S, García-Patrón R, Cerf N, Ralph T, Shapiro J and Lloyd S 2012 Gaussian quantum information *Mod. Phys.* **84** 621

[49] Peschel I 2003 Calculation of reduced density matrices from correlation functions *J. Phys. A* **36** L205

[50] Audenaert K, Eisert J, Plenio M and Werner R 2002 Entanglement properties of the harmonic chain *Phys. Rev. A* **66** 042327

[51] Plenio M, Eisert J, Dreissig J and Cramer M 2005 Entropy, entanglement and area: analytical results for harmonic lattice systems *Phys. Rev. Lett.* **94** 060503

[52] Cramer M, Eisert J, Plenio M and Dreissig J 2006 An entanglement-area law for general bosonic harmonic lattice systems *Phys. Rev. A* **73** 012309

[53] Schuch N, Cirac I and Wolf M 2006 Quantum states on harmonic lattices *Commun. Math. Phys.* **92** 65

[54] Banchi L, Braunstein S and Pirandola S 2015 Quantum fidelity for arbitrary Gaussian states *Phys. Rev. Lett.* **115** 260501

[55] Arias R, Casini H, Huerta M and Pontello D 2017 Anisotropic Unruh temperatures *Phys. Rev. D* **96** 105019

[56] Di Giulio G, Arias R and Tonni E 2019 Entanglement hamiltonians in 1D free lattice models after a global quantum quench *J. Stat. Mech.* 123103

[57] Baranov M 2024 Reduced density matrix and entanglement Hamiltonian for a free real scalar field on an interval (arXiv:2412.13777)

[58] Cardy J, Castro-Alvaredo O and Doyon B 2008 Form factors of branch-point twist fields in quantum integrable models and entanglement entropy *J. Stat. Phys.* **130** 129

[59] Mintchev M and Tonni E 2022 Modular conjugations in 2D conformal field theory and holographic bit threads *J. High Energy Phys.* JHEP12(2022)149

[60] Calabrese P, Cardy J and Tonni E 2012 Entanglement negativity in quantum field theory *Phys. Rev. Lett.* **109** 130502

[61] Calabrese P, Cardy J and Tonni E 2013 Entanglement negativity in extended systems: a field theoretical approach *J. Stat. Mech.* 02008

[62] Calabrese P, Cardy J and Tonni E 2015 Finite temperature entanglement negativity in conformal field theory *J. Phys. A* **48** 015006

[63] Peres A 1996 Separability criterion for density matrices *Phys. Rev. Lett.* **77** 1413

[64] Vidal G and Werner R 2002 Computable measure of entanglement *Phys. Rev. A* **65** 032314

[65] Murciano S, Vitale V, Dalmonte M and Calabrese P 2022 Negativity Hamiltonian: an operator characterization of mixed-state entanglement *Phys. Rev. Lett.* **128** 140502

[66] Parisen Toldin F and Assaad F F 2018 Entanglement Hamiltonian of interacting fermionic models *Phys. Rev. Lett.* **121** 200602

[67] Rottoli F, Murciano S, Tonni E and Calabrese P 2023 Entanglement and negativity Hamiltonians for the massless Dirac field on the half line *J. Stat. Mech.* 013103

[68] Estienne B, Ikhlef Y, Rotaru A and Tonni E 2024 Entanglement entropies of an interval for the massless scalar field in the presence of a boundary *J. High Energy Phys.* JHEP05(2024)236

[69] Tonni E, Rodríguez-Laguna J and Sierra G 2018 Entanglement hamiltonian and entanglement contour in inhomogeneous 1D critical systems *J. Stat. Mech.* 043105

[70] Bonsignori R and Eisler V 2024 Entanglement Hamiltonian for inhomogeneous free fermions *J. Phys. A* **57** 275001

[71] Bernard P, Bonsignori R, Eisler V, Parez G and Vinet L 2024 Entanglement Hamiltonian and orthogonal polynomials (arXiv:2412.12021)

[72] Wen X, Ryu S and Ludwig A 2018 Entanglement hamiltonian evolution during thermalization in conformal field theory *J. Stat. Mech.* 113103

[73] Rottoli F, Scopa S and Calabrese P 2022 Entanglement Hamiltonian during a domain wall melting in the free Fermi chain *J. Stat. Mech.* 063103

[74] Rottoli F, Rylands C and Calabrese P 2025 Entanglement Hamiltonians and the quasiparticle picture *Phys. Rev. B* **111** L140302

[75] Travaglino R, Rylands C and Calabrese P 2025 Quasiparticle picture for entanglement hamiltonians in higher dimensions *J. Stat. Mech.* 033102

[76] Läuchli A 2013 Operator content of real-space entanglement spectra at conformal critical points (arXiv:1303.0741)

[77] Surace J, Tagliacozzo L and Tonni E 2020 Operator content of entanglement spectra in the transverse field Ising chain after global quenches *Phys. Rev. B* **101** 241107(R)

[78] Huerta M and van der Velde G 2023 Modular Hamiltonian of the scalar in the semi infinite line: dimensional reduction for spherically symmetric regions *J. High Energy Phys.* JHEP06(2023)097

[79] Huerta M and van der Velde G 2024 Modular Hamiltonian in the semi infinite line. Part II. Dimensional reduction of Dirac fermions in spherically symmetric regions *J. High Energy Phys.* JHEP01(2024)062

[80] Mintchev M, Pontello D, Sartori A and Tonni E 2022 Entanglement entropies of an interval in the free Schrödinger field theory at finite density *J. High Energy Phys.* JHEP07(2022)120

[81] Mintchev M, Pontello D and Tonni E 2022 Entanglement entropies of an interval in the free Schrödinger field theory on the half line *J. High Energy Phys.* JHEP09(2022)090

[82] Eisler V 2024 Entanglement Hamiltonian of a nonrelativistic Fermi gas *Phys. Rev. B* **109** L201113

[83] Eisler V 2025 On the Bisognano–Wichmann entanglement Hamiltonian of nonrelativistic fermions *J. Stat. Mech.* 013101

J. Stat. Mech. (2025) 073102